

Air-Powered Liquid Needle Free Injectors: Design, Modeling and Experimental Validation

Rocco Portaro

A Thesis

in

The Department

of

Mechanical and Industrial Engineering

Presented in Partial Fulfillment of the Requirements

For the Degree of Master of Applied Science (Mechanical Engineering) at

Concordia University

Montreal, Quebec, Canada

February 2013

CONCORDIA UNIVERSITY
School of Graduate Studies

This is to certify that the thesis prepared

By: Rocco Portaro

Entitled: Air-Powered Liquid Needle Free Injectors: Design, Modeling and Experimental Validation

and submitted in partial fulfillment of the requirements for the degree of

Master of Applied Science (Mechanical Engineering)

complies with the regulations of the University and meets the accepted standards with respect to originality and quality.

Signed by the final examining committee:

Dr. A. K. Waizuddin Ahmed Chair

Dr. Lyes Kadem Examiner

Dr. Liangzhu (Leon) Wang Examiner

Dr. Hoi Dick Ng Supervisor

Approved by _____
Chair of Department or Graduate Program Director

Dean of Faculty

Date February 26, 2013

Abstract

Air-Powered Liquid Needle Free Injectors: Design, Modeling and Experimental Validation

Rocco Portaro

Liquid needle free injectors are biomedical devices that deliver medication via the creation of high speed liquid jets without the use of hypodermic needles, have been a topic of interest in the scientific community for quite some time. This study focuses on the development and analysis of liquid jet injectors powered by air. Studies demonstrate that the majority of commercially available injectors are gas/air powered units; however there is no indication of a model that prescribes the performance characteristics of this particular type of injector. Consequently the main goal of this research is to develop and validate a model capable of predicting the behaviour of such devices.

In this study, the development and analysis of a model for air-powered injectors is accomplished first by constructing a prototype injector that functions in a very similar fashion and produces jets of similar geometry and velocities as the vast majority of commercially available units. Furthermore, the injector is designed in such a way that the parameters such as, driver pressure, injection chamber length and volume as well as nozzle geometry can be varied.

An initial evaluation of the prototype injector is performed to ensure it can be used to accurately conduct testing. The prototype injector is then used to validate a fluid mechanics model constructed based on previous work from Baker and Sanders [IEEE Trans. Biomed. Eng. 46:235-242, 1999]. Experiments that map stagnation pressures of the jet through the use of a piezoelectric force transducer are performed in order to validate the performance of the model. These experiments describe the peak and average stagnation pressures of the jet based on the effect of different parameters such as driver pressure (400-800 kPa), nozzle size (130-250 μm) and injection chamber length (10-25 mm). The results of these tests are then compared to the behaviour prescribed by the model. An analysis of these results indicates that the present model can accurately be used to predict the performance of air-powered needle free liquid jet injectors.

Acknowledgements

I would first like to thank Dr. Hoi Dick Ng who sparked my interest in conducting research and has helped guide me through my academic career. I am extremely grateful for the hard work, dedication and support which he provides.

I am also very grateful to have such great laboratory colleagues; especially Haruka Nakayama and Anna Chtchetinina who have helped me complete my research by offering their assistance in conducting my not so glamorous experiments.

Finally, I would like to thank my parents who have taught me the value of hard work and discipline, and have supported me all these years through my many endeavours. My sister, Cathy who has always been there for me to help guide and provide encouragement all these years, as well as for proofreading every paper I wrote. I would also like to thank Kamila, for believing in me and being very supportive, the warm coffees you brought me when things were rough will never be forgotten.

Table of Contents

Table of Contents	v
List of Figures	vii
List of Tables	ix
Nomenclature	x
Chapter 1. Introduction	1
1.1. General Overview	1
1.2. Motivation.....	1
1.3. Skin Anatomy and Physiology.....	4
1.3.1. The Epidermis.....	6
1.3.2. The Basement Layer	9
1.3.3. The Dermis and Subcutaneous Tissue	10
1.4. Drug Absorption by Needle Free Liquid Jet Injection across Skin	11
1.5. Potential Drugs to be administered via Needle Free Injection.....	14
1.6. Skin Mechanics.....	15
1.7. Liquid Jet Fluid Dynamics.....	22
1.8. Needle Free Liquid Jet Injector State-of-the-Art Technologies.....	29
1.9. Objective of the present work.....	32
Chapter 2. Prototype and Physical Model	34
2.1. Prototype Design of the Injector	34
2.2. Model Describing Air-powered Injectors	39
2.3. Motion Analysis.....	43
2.4. Driving Force.....	44
2.5. Friction and Damping Forces.....	45
2.6. The Complete Model	53
Chapter 3. Results and Discussion	58
3.1. Qualitative Assessment.....	58
3.2. Quantitative Assessment.....	63
3.2.1. Test Procedure	66
3.3. Results.....	67
Chapter 4. Conclusion	84
4.1. Concluding Remarks.....	84

4.2. Contribution to Knowledge.....	85
References	86
Appendix	88

List of Figures

Figure 1.1. Various needle free drug technologies (Mitragotri 2005)	2
Figure 1.2. Skin anatomy and physiological aspects (Brown <i>et al.</i> 2006).....	5
Figure 1.3. Cross-section of epidermis (Kendall 2010)	6
Figure 1.4. Detailed skin anatomy (Kendall 2010).....	10
Figure 1.5. Skin crack model parameters (Shergold <i>et al.</i> 2005).....	17
Figure 1.6. Minimum pressure to puncture skin versus jet diameter (Shergold <i>et al.</i> 2005).....	18
Figure 1.7. Planar crack formation in a) skin; and b) silicone rubber (Shergold <i>et al.</i> 2005).....	19
Figure 1.8. a) Delivery efficiency versus power; and b) penetration versus power (Mitragotri 2006)	21
Figure 1.9. Geometries considered by Seehanam <i>et al.</i> (2009)	23
Figure 1.10. Pressure as a function of time for step-like geometry (Seehanam <i>et al.</i> 2009)	24
Figure 1.11. Pressure as a function of time for a conical geometry (Seehanam <i>et al.</i> 2009).....	24
Figure 1.12. Comparison of experimental and theoretical results for nozzle pressure (Seehanam <i>et al.</i> 2009).....	25
Figure 1.13. Maximum pressure as a function of parameter sensitivity by Baker and Sanders (1999).....	26
Figure 1.14. Time required for maximum pressure from parameter sensitivity by Baker and Sanders (1999)	27
Figure 1.15. Production of highly focused jet (Tagawa <i>et al.</i> 2012)	28
Figure 1.16. Typical layout of commercial injectors (Tev-Tropin Inc.).....	29
Figure 1.17. Schematic for gas powered injector (Shergold <i>et al.</i> 2005).....	30
Figure 2.1. Schematic of prototype injector.....	36
Figure 2.2. Penetration of prototype injector into polyacrylamide gel at a driver pressure of 700 kPa	39
Figure 2.3. Experimental pressure trace for spring powered injector obtained by Chen <i>et al.</i> (2011).....	42
Figure 2.4. Spring rate as a function of maximum stagnation pressure obtained by Chen <i>et al.</i> (2011).....	43
Figure 2.5. Driver chamber geometry	44
Figure 2.6. Cross-section of venting chamber	46
Figure 2.7. O-ring friction parameters	47
Figure 2.8. O-ring wedge geometry	51

Figure 2.9. O-ring load per linear in of seal as a function of compression fit (Darcoïd 2013).....	52
Figure 2.10. Numerical simulation of jet stagnation pressure	54
Figure 2.11. Numerical simulation of jet velocity	55
Figure 2.12. Numerical simulation of driver/piston velocity and displacement	56
Figure 3.1. Penetration into bloom 250 ballistics gel with 200 μm nozzle.....	59
Figure 3.2. Cross-section of penetration test on 20 mm thick bovine meat with 200 μm nozzle and 0.1 ml of injection volume.....	59
Figure 3.3. Penetration depth into bloom 250 10% wt. gel as a function of driver pressure	60
Figure 3.4. High speed photography of liquid jet with 180 μm nozzle and at 700 kPa driver pressure	61
Figure 3.5. Numerical results illustrating liquid fraction of jet (courtesy of H. Nakayama)	63
Figure 3.6. Experimental setup of injector on force transducer.....	65
Figure 3.7. Stagnation pressure as function of injection time for 200 μm nozzle at 413 kPa.....	68
Figure 3.8. Jet velocity as a function injection time for 200 μm nozzle at 413 kPa	70
Figure 3.9. Peak stagnation pressure as a function driver pressure	71
Figure 3.10. Average stagnation pressure as a function driver pressure.....	72
Figure 3.11. Stagnation pressure as a function time without fluid damping in the model.....	74
Figure 3.12. Stagnation pressure as a function time with fluid damping in the model.....	74
Figure 3.13. Effect of stand-off distance on stagnation pressure.....	75
Figure 3.14. No stand-off distance causing inaccurate results.....	77
Figure 3.15. Effect of injection chamber length on stagnation pressure.....	78
Figure 3.16. Effect of injection volume on overall injection time	78
Figure 3.17. Peak stagnation pressure as a function of chamber length for 129 μm nozzle and 580 kPa driver pressure.....	80
Figure 3.18. Average stagnation pressure as a function of chamber length for a 129 μm nozzle and 580 kPa driver pressure.....	80
Figure 3.19. Effect of O-ring friction on stagnation pressure.....	82

List of Tables

Table 1.1. Examples of drugs administered via liquid jet injector (Mohanty <i>et al.</i> 2011).....	14
Table 1.2. Commercially available injectors and corresponding power source (Mohanty <i>et al.</i> 2011)	32
Table 2.1. Prototype injector parameters	38
Table 2.2. Compression load produced by O-rings within injector body	52
Table 3.1. Nozzle number and size specifications	66
Table 3.2. Experimental test parameters	66
Table 3.3. Error for peak stagnation pressure measurements	71
Table 3.4. Error for average stagnation pressure measurements	73

Nomenclature

List of Symbols

A_D	area of driver piston (m^2)
A_o	area of nozzle orifice (m^2)
A_p	area of plunger situated in injection chamber (m^2)
B	bulk modulus of fluid in the injection chamber (N/m^2)
D	inner diameter of O-ring seal (mm)
F_{fluid}	force of fluid exerted on O-ring due to p_r (N)
f_{O-ring}	force exerted on O-ring due to p_{O-ring} (N)
h	height of clearance gap used for O-ring (mm)
h_c	height of maximum pressure in O-ring clearance gap (mm)
L	length of liquid injection chamber (mm)
L_o	initial length of driver chamber (mm)
m_a	mass of air in driver chamber (kg)
M	mass of driver/plunger assembly (kg)
p	pressure of liquid within injection chamber (MPa)
p_{O-ring}	complete pressure distribution on O-ring (MPa)
p_r	pressure distribution acting on O-ring within clearance gap (kPa)
Q	volumetric flow rate (m^3/s)
u_p	liquid velocity at plunger interface (m/s)
u_o	liquid velocity at nozzle exit orifice (m/s)
v	fluid velocity at used to compute volumetric flow rate (m/s)
Vol_D	volume of driver chamber (m^3)
X_p	displacement of piston from start time of injection (mm)
f_c	force produced due to O-ring compression in housing (N)

Greek Symbols

ρ_o initial density of liquid in injection chamber (kg/m^3)

ρ density of liquid in injection chamber (kg/m^3)

$\Delta\rho$ incremental change of liquid density in injection chamber (kg/m^3)

Dimensionless Parameters

Re Reynolds Number

Chapter 1. Introduction

1.1. General Overview

Although the needle free liquid jet injector, a device that delivers medication without the use of a hypodermic needle has been developed for many years, the full potential of this engineering device has not been fully realized. It is known that the successful development depends on the full understanding of the physical processes inside the device. The small scale of the phenomenon makes this challenging to describe. In the present thesis, the objective is to contribute to a better description of the needle free injector and in particular to provide a theoretical model for air powered injectors as well as investigate the influence of different physical parameters.

1.2. Motivation

In today's rapidly growing society a greater emphasis is placed on providing the most efficient and comfortable health care to patients. In fact, many new medical breakthroughs have resulted from increased interest in improving health care. The advent of minimally invasive and robotic surgery, has led to operations which are safer, more effective and lead to less recovery time. Medical imaging techniques have also made great leaps; magnetic resonance imaging can now be used to completely map one's anatomy in three dimensions, helping doctors make more accurate diagnosis. However, one medical technique that has been unchanged for centuries is that of drug delivery using hypodermic needles. This basic technique consists of puncturing the skin with a hollow metal tube, whereby the end is cut at an angle in order to form a sharp point. Once the tube is inserted to an adequate depth, usually reaching past the dermis of the skin,

then medication is pumped through the needle by depressing a plunger attached to a syringe assembly which holds the needle in place.

Although there have been many improvements in reducing the diameter of needles there exist many drawbacks. These include accidental needle stick injuries and the re-use of needles which happens in developing countries due to the lack of funding for medical supplies. These scenarios can lead to the transmission of deadly viruses, such as HIV. Moreover, the phobia of needles among many patients has led to their non compliance of medical treatment, which can seriously compromise their well being. Lastly, with over 12 billion needle injections performed worldwide every year, the safe disposal of the used needles becomes a difficult undertaking (Mitragotri 2006). Consequently it is important to investigate new alternative methods for drug delivery.

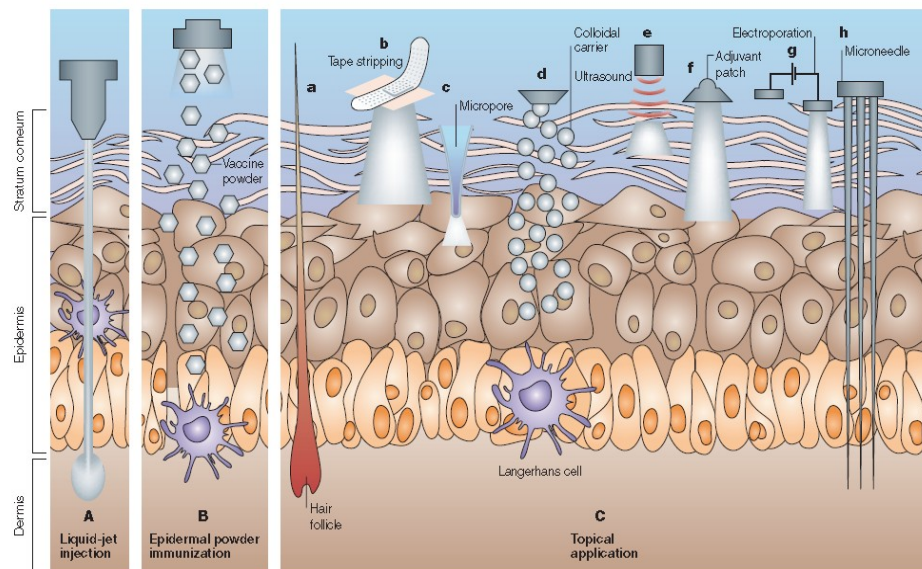


Figure 1.1. Various needle free drug technologies (Mitragotri 2005)

Needle free injections have been a topic of interest in the scientific community for quite some time; in fact there exist a number of techniques that can be utilized to effectively deliver medication to the different layers of skin. Figure 1.1 provides some examples of these techniques which include electroporation and ionization, that utilize electric current to enlarge skin pores, as well as ultrasound, laser and photomechanical waves (Mitragotri 2005). These technologies are capable of delivering medication without directly puncturing the skin. However a brief overview of these technologies will demonstrate that there exist several limitations in the ability to deliver macro molecules due to the limit that a skin pore can be enlarged, as well as the need to deliver the medication in a reasonably short time frame (Mitragotri 2005). Consequently it is necessary to develop a technology which will puncture the surface of the skin and deliver a broader range of medication in a similar fashion to a hypodermic needle. This must be accomplished in way that will reduce pain, eliminate biological waste and reduce the risk of cross contamination between patients.

In order for the medical community to solve the problem plaguing hypodermic needles, they turned to the field of fluid dynamics. It was established that a small diameter liquid jet of sufficient pressure could penetrate the skin and deliver the appropriate amount of medication. In the late 1800's these high powered jets were used in what was termed "aqua puncture" therapy (Mitragotri 2006). These rudimentary devices were used to deliver water and other liquids for the treatment of conditions such as uncontrolled neuralgia. Consequently, the primary goal of these devices was not that of delivering medication but as a means to treat disorders. The development of jet injectors for the administration of medication began in the early 1930's where it was

necessary to have a very quick and effective way to immunize the masses against diseases such as polio, influenza, smallpox. The early jet injectors allowed medical professionals to quickly vaccinate the masses at a rate of up to 1000 immunizations per hour (Mitragotri 2006). Nevertheless there were major drawbacks that were detrimental towards their wide spread use. The most obvious was that the injections resulted in more pain and bruising than conventional hypodermic needles. More importantly, it was observed that there was cross contamination between patients, due to the splash back of fluids on to the injector tip over multiple injections. Consequently, these early jet injectors exacerbated the problems they set out to solve, rather than improving the current drug delivery techniques.

Despite the problems encountered with the early use of liquid jet injectors, much research has been conducted on improving their performance and developing marketable prototypes. Observing the physiology and anatomy of the skin and developing models to characterize skin mechanics as well as liquid jet impingement on the skin surface has led greatly to the evolution of a viable needle free injector liquid jet injector.

1.3. Skin Anatomy and Physiology

The goal of needle free liquid jet injections is to puncture human skin and deliver large macromolecules, while minimizing damage to the skin caused by the injection. In order to accomplish this objective it is necessary to have a general understanding of skin anatomy as well as the physiology of drug absorption through the different parts of the skin.

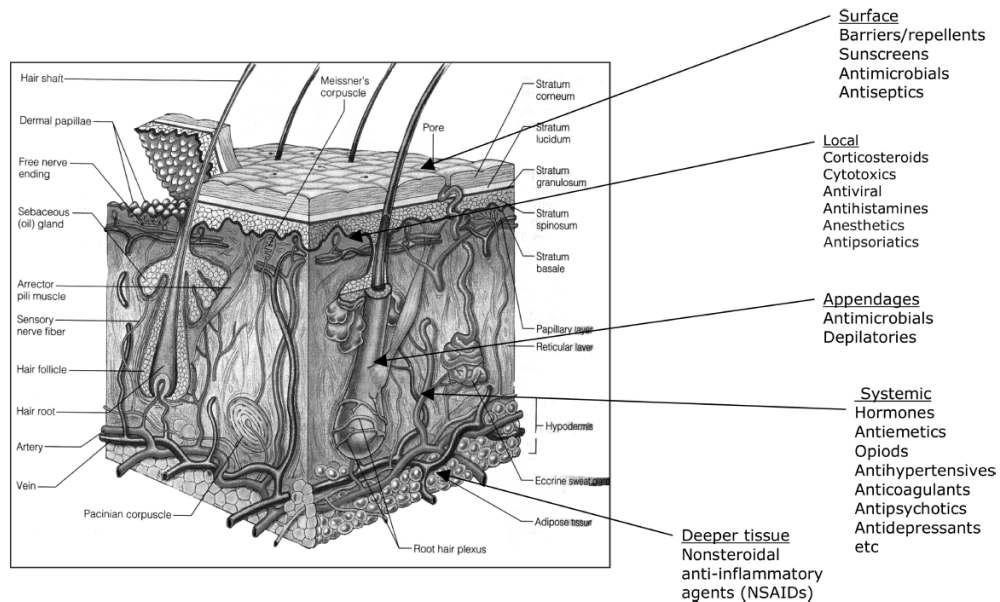


Figure 1.2. Skin anatomy and physiological aspects (Brown *et al.* 2006)

The human skin is the body's largest organ and is composed of three main parts: the epidermis which comprises the skin's outermost layer, the dermis which lies beneath the epidermis and is a fibre-like network of protein, and finally the subcutaneous tissue composed mainly of fat. The skin has complex anatomical and physiological aspects, which vary greatly with location on the human body. For example, the thickness of the epidermis and dermis can change substantially from one location to another. This can be seen by observing the thickness of the epidermis on the eye lid which measures just 0.1 mm and comparing it to the thickness of the epidermis on the sole of the foot which measure almost 1.5 mm (McGrath *et al.* 2010). Understanding these variations is essential in developing an injector that has the capability to deliver medications to different parts of the body.

1.3.1. The Epidermis

The Epidermis is the skin's outermost layer and is comprised of two types of cells, keratinocytes and dendrite cells. Keratinocytes comprise 80% of the epidermal layer and are long thread like proteins which help protect the body against external chemical, physical and biological risks. The dendrite cells found in the epidermis take the form of Langerhans, which act as antigen processing units. Basically, when a foreign substance is detected the Langerhans cells become active and migrate to lymph nodes where they provoke an immunological response. The epidermis also contains other auxiliary cells such as melanocytes and Merkel cells which also play a protective role and help give the skin its pigmentation (Kolarsick *et al.* 2011). Figure 1.3 illustrates a cross section of the epidermis, which is divided into four distinct layers, consisting of the cornified layer, the granular layer, the squamous and the basal layer.

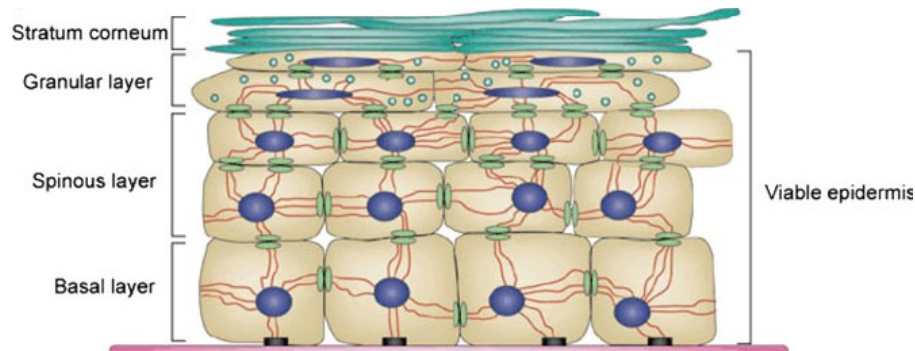


Figure 1.3. Cross-section of epidermis (Kendall 2010)

The cornified layer (stratum corneum) is the most superficial layer of the epidermis and consists of corneocytes cells which provide mechanical protection against external elements. The corneocytes are dead skin cells due to the fact that they have lost their nuclei through a process termed “terminal differentiation”. The cornified layer of the epidermis is extremely high in protein content due fact that it must exhibit mechanical

toughness. Furthermore, the properties within the cornified layer vary greatly with depth. This is the case with the water binding capacity of the corneocytes which increases as the cornified layer is traversed. Consequently, as the corneocytes makes its way up to the surface it dehydrates and eventually flakes off the skin (Kolarsick *et al.* 2011). A needle free injector must provide enough force to penetrate through the 15 to 20 layers of these dead skin cells. This is no trivial task as the thickness of this layer can vary substantially from 5 to 20 μm (Bermejo and Gonzalez-Alvarez 2008). Further complicating matters is the fact that the breaking stress of this layer varies significantly with ambient humidity. In fact studies have demonstrated that the breaking stress of this layer can vary from 22.5 MPa at 0% humidity to 3.2 MPa at 100% humidity. The breaking stress also decreases with increasing depth within the layer (Kendall 2010).

The next layer of the epidermis beneath the cornified layer is known as the granular layer. This layer is proportional in thickness to the cornified layer and is the last layer of the skin to contain living cells. In fact it is in the granular layer whereby the keratinocytes undergo terminal transformation in order to become corneocytes, which is carried out in part by enzymes found in this layer. Furthermore, the granular layer also contains keratohylaine cells which are used in the synthesis of various proteins (Kolarsick *et al.* 2011).

Immediately preceding the granular layer is the squamous layer, referred to as the stratum spinosum. This layer is composed of polyhedral shaped keratinocytes approximately 5 to 10 cells in thickness. The main role of the squamous layer is in the synthesis of proteins such as cytokeratin. The cytokeratin combines with cytoplasmic

proteins also found within the squamous layer, in order to form desmosomes. The desmosomes provide a strong linking agent between keratinocytes (Kolarsick *et al.* 2011).

The final layer of the epidermis is known as the basal layer, this layer is characterized by long column shaped keratinocyte cells that attach with their long axis perpendicular to a junction layer between the epidermis and the dermis known as the basement layer. The basal layer also contains mitotically active cells, which means the cell division and cell growth takes place within this layer. It typically requires 14 days for a newly developed cell within the basal layer to undergo a complete cycle and become a corneocyte (McGrath *et al.* 2010).

It is important to note the epidermis is constantly evolving and as such can be considered a “dynamic layer”, cells are travelling from the basal layer up to the cornified layer and they eventually flake off the skin. This process of cell traveling through the various layers of the epidermis is termed keratinization. The cell first undergoes a period of synthesis while it travels through the basal and squamous layer. During this period the cell builds up a cytoplasmic supply of keratin that serves as the cells cytoskeleton. The degradation phase takes place in the granular layer and cornified layer, whereby the cells do not synthesis rather they lose organelles until even the cell nucleus is removed. The cells are then considered dead and at this point have migrated to the outer most part of the epidermis (Kolarsick *et al.* 2011). Consequently each layer of the epidermis plays an important role in skin regeneration as well as protecting the body from external hazards.

It is of extreme importance to consider this dynamic behaviour of the skin when designing a needle free liquid injector. This is because in order for the injector to deliver

medication it must wound the skin, in other words it must make a hole which will not heal instantaneously, introducing an entry point for external elements to enter the body. Consequently it is important to understand the mechanisms the skin has in place for providing protection as well as the length of time it takes for wounds to heal and regain original skin properties.

1.3.2. The Basement Layer

The basement layer is a junction between the epidermis and the dermis; it is an extremely important part of the skin anatomy and has many specialized roles. It helps establish cell polarity, direction of growth, provides development signals and acts as a semi permeable layer (Kolarsick *et al.* 2011). The basement layer consists of porous zone that allows fluid exchange between the dermis and epidermis and also forms a support structure that holds the epidermis to the dermis. Among the many cells found within this junction zone, the basal keratinocytes are of particular importance. This is because they are the cell which will form anchoring fibrils and micro fibrils that will transfer shearing and tensile forces from the epidermis to the dermis (McGrath *et al.* 2010).

1.3.3. The Dermis and Subcutaneous Tissue

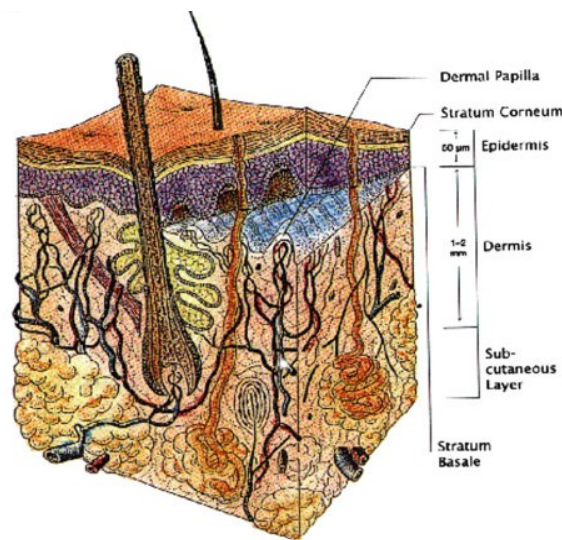


Figure 1.4. Detailed skin anatomy (Kendall 2010)

The dermis is found beneath the epidermis and the basement layer; it comprises the bulk of the skin and is composed primarily of collagen (70% dry wt.). Collagen has similar mechanical properties to nylon and aids in giving skin its pliability, elasticity and tensile strength (McGrath *et al.* 2010). Consequently, the dermis serves to protect the body against mechanical injury, in contrast to the epidermis which serves to seal the skin from external chemical and biological hazards. Moreover, the dermis exhibits a clear structural arrangement of components that are predictable in a depth-wise manner and the cells within the dermis do not undergo a differentiation process. Fibrous filaments, amorphous connective tissue, nerve endings and vascular networks can also be found in the dermis. Below the dermis it is possible to locate the subcutaneous tissue, which is composed mainly of fat. In this layer it is possible to find blood vessels, lymphatic vessels and even nerve endings (Kolarsick *et al.* 2011). It is important to note that this is

the layer of the skin that is targeted for the delivery of hormones using conventional hypodermic needles. This is because minimal pain is sensed by inserting objects into this region. The subcutaneous tissue can be considered the final layer of skin, directly beneath it is the muscular tissue. Therefore needle free liquid injectors must also have the ability to penetrate into these layers of the skin in order to deliver medication developed to function with these tissues.

Understanding the structure of the skin is fundamental in creating a needle free injector that will function efficiently and painlessly. The above description of the skin makes it possible to observe that it is possible to inject into the epidermis or basement layer without causing any sensation of pain. This is because nerve endings begin to be present in the dermal layer. Moreover, once injected through the epidermis the medication will diffuse into the dermis and subsequently be absorbed by the body. Consequently it is also necessary to introduce the mechanisms at play in order to absorb the medication injected into the body.

1.4. Drug Absorption by Needle Free Liquid Jet Injection across Skin

There are two routes by which drugs can be administered to the human body these are parenteral and enteral. A drug administered to the body which is absorbed in the intestinal tract is considered as an enteral route for absorption, while a drug administered from outside the body that makes its way directly to the blood stream is considered parenteral. Consequently, an injection given by a needle free injector is parenteral. This is due to the fact that a liquid jet punctures the skin and makes a depot of medication at some specific depth where it then diffuses into the blood stream (Bermejo and Gonzalez-Alvarez 2008).

The conventional hypodermic needles target three specific areas for drug absorption these include intra dermal, subcutaneous and intramuscular sites. Needle free injectors can also target these specific zones and also have the advantage of targeting sites which are much shallower than those used by conventional hypodermic needles. The drug absorption from these shallow injection depths is termed trans-dermal absorption. It is important to understand the intricacies of the more common injection sites as well as the newly targeted areas in order to design a versatile needle free injector.

The typical injection sites include intra dermal, subcutaneous and intramuscular regions. Intradermal injections consist of depositing medication into the dermis which is rich in capillaries. The medication then diffuses from the initial deposit site to the blood capillaries and then makes its way in to systemic circulation. It is important to note that the maximum volume that can be administered via this technique is 0.1 ml. Subcutaneous injections are usually performed at depths just below the dermis into the fatty tissue. The maximum volume of liquid that can be injected within this region is 2 ml. Moreover, the absorption rate can be increased by massaging the injection rejoin once the injection is performed. This forces the concentrated deposit of medication to spread out and make more contact with blood capillaries (Bermejo and Gonzalez-Alvarez 2008). Intramuscular injections consist of depositing medication within the muscular tissue. Although this is a painful event due to the sensory nerves found within this region, there also exists quite an extensive blood supply which leads to very rapid absorption. The maximum volume that can be injected intramuscularly varies depending on the body site typically from 2 ml to 15 ml. Regardless of the injection site; there are only two mechanisms that govern drug absorption for these three regions. Once the medication has been delivered it can either

travel through lymphatic vessels, or capillaries. The method is dependent on the molecular weight of the drug. If it is greater than 2000 Daltons the drug will be absorbed by the lymphatic system; if it is less then it will be absorbed by blood capillaries. It is important to note that the surface of capillaries is covered with pores. The absorption rate of the drug into systemic circulation is dependent upon its ability to diffuse into these pores. The rate at which the medication diffuses into the pores is governed by Fick's law,

$$\frac{dQ}{dt} = \left(\frac{D \cdot p \cdot S}{L \cdot V_a} + \frac{D' \cdot S'}{\eta \cdot L' \cdot V_a} \right) Q_a \dots \text{Fick's Law}$$

where dQ/dt is the absorption rate of the drug, Q_a is the amount of drug in the injection region, and the other coefficient depend on the properties of skin.

Transdermal injections are performed by depositing medication into the epidermis, typically under the cornified layer, and relying on passive diffusion to transport the medication into systemic circulation. Although absorption is slower due to the fact that drugs administered in this way must make their way into the dermis before entering the blood supply, there is much research into using this area for vaccination purpose. This is because the epidermis contains Langerhans cells which provoke immunological responses. Consequently it was established that vaccinations targeted in this region were much more effective than those administered in the intramuscular region. It is also very important to note that targeting these shallow depths via the use of needles is extremely difficult, however with the use of needle free injectors it is possible not only to target conventional injection zones but to explore the development of more efficient vaccines and hormones designed to work at an epidermal level (Kendall 2010).

1.5. Potential Drugs to be administered via Needle Free Injection

Needle free injectors, have the ability to deliver large scale macro molecules, which makes them much more appealing than other types drug delivery. In fact, needle free injectors can deliver the same types of medications as conventional hypodermic needles. There are a few sectors of the medical field where needle free injectors can be of particular use. The first is for the treatment of chronic diseases such as diabetes. Diabetics must take insulin with the use of a hypodermic needle that targets the subcutaneous layers of the skin. Needle free injectors that are commercially available have shown that they can lead to greater insulin absorption rates due to the fact that insulin is more dispersed within the tissue. Growth hormones are yet another key area that has seen success with needle free injectors. This is due to the fact that most of the patients requiring growth hormone therapy are children and adolescents, consequently using a needle free injectors eliminates the phobia associated with needles and helps patients comply with their treatment.

Medication Delivered Via Needle Free Injection	
Drug	Usage
Vaccines	Immunization
Insulin	Blood Sugar Control
Growth Hormones	Increase Growth Rate
Lidocaine	Anesthetic
Midazolam	Sedative
Erythroprotein	Proteins for DNA Therapy
Interferon	
Botulinum Toxin	

Table 1.1. Examples of drugs administered via liquid jet injector (Mohanty *et al.* 2011)

Needle free injectors are also proving to be extremely useful in new types of treatments such as DNA therapy. The injectors are used to deliver specific proteins to epidermal layers of the skin, which as previously described control many immunological responses through Langerhans cells. Conventional ways of targeting these epidermal tissues consist of using micro needles arrays. These are extremely small diameter needles that have the ability to deliver medication at shallow depths, however they are extremely costly to manufacture and difficult to use. The needle free injector provides bioengineers with a means of delivering these DNA therapies in a much quicker and efficient manner (Brown 2006).

1.6. Skin Mechanics

Although there is a vast array of medication that can be delivered by needle free injection with better absorption capabilities than hypodermic needles, needle free injectors have not seen widespread use. There exist a number of reasons that have limited needle free injectors from replacing the hypodermic needle. The major setbacks include pain, bruising, hematomas, incomplete delivery of medication, excessive penetration and cross contamination when multiple use injectors are invoked for vaccination purposes (Mitragotri 2006). Despite these issues, if the needle free injection process is analyzed from an engineering perspective then it may be possible to alleviate or eliminate most of these problems.

In order to deposit medication in one of the various layers of the skin, it is necessary to puncture the skin in order to create a hole through which the medication will flow and deposit. Needle free injectors accomplish this by utilizing the medication itself to form a high speed liquid jet that punctures the skin. The liquid jet that is emitted from needle

free injectors typically has two phases, the first consists of a high pressure and velocity phase whereby the liquid jet penetrates the skin and the second phase consists of a lower velocity deposition phase where the drug is delivered to the target tissue. Substantial work has been conducted on determining various models to characterize both injection phases.

In the first phase of injection the liquid jet must penetrate the skin, which can be considered a highly viscous elastic material, with anisotropic properties. A very successful skin fracture model has been developed by Shergold *et al.* (2005). Their model not only describes the fracture mechanism at play when the liquid jet penetrates the skin, but can also be used to predict the minimum stress required to puncture human flesh with regards to jet diameter. In fact in their research Shergold *et al.* used commercially available injectors in order to validate their results as well as to evaluate the performance of different injectors.

The basic model proposed by Shergold *et al.* (2005) compares the penetration of a liquid jet through skin to the fracture mechanics exhibited by a sharp tipped punch through a soft solid material. In fact, this study suggests that the fracture mechanism can be explained by a Mode I crack propagation failure mode whereby a hole is formed due to the appearance of a planar crack. It also suggests that crack formation should be analyzed in term of energy. The skin can be considered as a hyper-elastic, anisotropic, incompressible material; consequently the Ogden equation that describes strain energy density can be invoked to compute the force required to puncture the skin. This equation is given as:

$$\phi = \frac{2\mu}{\alpha^2} (\lambda_1^\alpha + \lambda_2^\alpha + \lambda_3^\alpha - 3)$$

where ϕ represents energy density per unit volume, μ represents the shear modulus, α is the strain hardening exponent and λ are the principal stretch ratios.

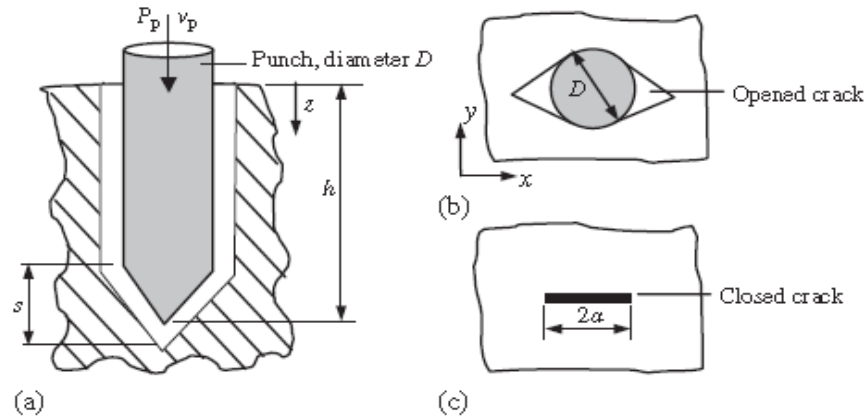


Figure 1.5. Skin crack model parameters (Shergold *et al.* 2005)

Shergold *et al.* used this model and determined that liquid jets follow a very similar behaviour, in fact as the diameter of the jet is diminished the pressure required to perforate the skin also increases. This increase is also dependent upon fracture toughness as well as shear modulus and strain hardening properties of skin. Shergold *et al.* used this model in conjunction with human experimentation in order to determine the minimum pressure required to puncture skin. A value of 14 MPa was established for a jet diameter of 0.34 mm. It is important to note that most of the jet injectors produce jets that range in diameter from 0.1 to 0.5 mm, and consequently the value established by Shergold *et al.* is a mid-range value. In order to further validate the “sharp punch model” samples of human skin were taken in order to test for strain hardening exponents, shear modulus and stretch ratios. These values were then used to plot a curve for the “sharp punch model” for a variety of jet diameters, as illustrated in Fig. 1.6.

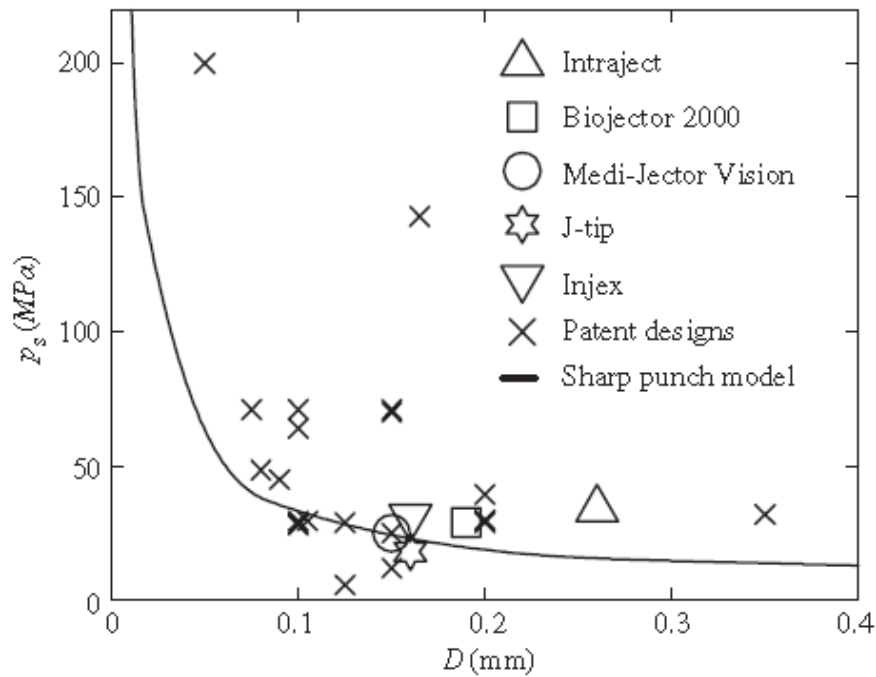


Figure 1.6. Minimum pressure to puncture skin versus jet diameter (Shergold *et al.* 2005)

Figure 1.6 illustrates the relationship between the minimum pressures required to perforate skin at a certain diameter for the theoretical sharp model, but also compares various commercially available injectors and their performance with respect to the “sharp punch model”. It is possible to see that the reputable injectors such as the Biojector, Injex and Medi-Jector Vision display a very good fit to the theoretical model.

Once the skin has been punctured, the liquid jet travels deeper into the various layers of skin where it eventually loses power and can no longer penetrate deeper. It is at this point in time where the medication begins to be deposited in a spherical manner just below the penetration zone. The depth that an injector can attain as well as the quantity of fluid it can deliver is dependent upon many factors. However it is first necessary to understand the process that the fluid undergoes to arrive at its target destination. The liquid jet will puncture the skin; this initial crack does not instantaneously become the

same size as the diameter of the jet. This is due to the fact that the puncturing process is governed by Mode I crack propagation and although the time for the small crack to propagate is short it is not instantaneous Shergold *et al.* (2005). Consequently, if the flow rate of the jet impinging on the skin is greater than the volumetric formation rate of the hole then medication splashes back towards the injector. Furthermore, fluid eventually fills the hole as it is being created, the incoming jets is then slowed down by the fluid and loses power. This in turn results in a loss in the ability of the jet to penetrate further into the skin. Once the jet can no longer penetrate deeper into the skin then it begins to deposit medication. The medication is accumulated in a sphere like shape around the point where the jet reached its terminal depth (Mitragotri 2006).

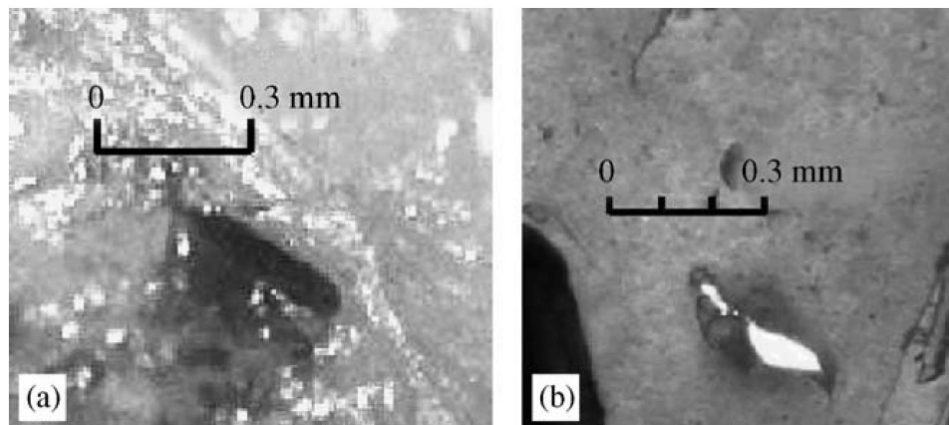


Figure 1.7. Planar crack formation in a) skin; and b) silicone rubber (Shergold *et al.* 2005)

The most crucial parameters in determining how deep a liquid jet injector will penetrate are the jet diameter, jet velocity as well as nozzle standoff distance, which describes how far from the skin the injector tip is placed. Studies have shown that in order to describe jet penetration these parameters must be lumped together and the jet

must be described in terms of power. In fact Schramm-Baxter *et al.* (2004) state that the power of a liquid jet formed by needle free injectors is given the following formula:

$$Power = \frac{1}{8} \pi \rho D^2 U^3 \quad \text{Eq. 1.1}$$

where ρ is the density of the fluid injected, D is the jet diameter and U is the velocity of the jet. Moreover, the power required to achieve a certain depth can vary greatly with different skin properties. In fact it was established that as the Young's modulus of skin increases, the power required to achieve a certain depth also increases dramatically. Schramm-Baxter *et al.* illustrated that an increase of 300% in Young's modulus made it possible to only deliver 10% of the intended injection at the targeted location (Schramm-Baxter *et al.* 2004).

Completeness of injection is another parameter which is used to measure the efficiency of the jet's penetration into the skin. This parameter measures the amount of fluid that makes it to the target tissue and compares it with the initial amount of fluid injected. A completeness of injection of 90% would indicate that 10% of the injection volume did not reach the target tissue. This is a very important notion, because it is necessary that the correct amount of medication is delivered in order to properly treat patients. As previously mentioned, when the jet begins to puncture the skin there exists some backplash as well as some loss that occurs due to the hole formation rate being smaller than the volumetric flow rate of the jet. In fact studies suggest that the completeness of injection also depends on the jet power. Mitragotri (2006) conducted a study which suggested that completeness of injection increases linearly with jet power, and exceeds 90% margin when the jet has a power greater than 30 watts.

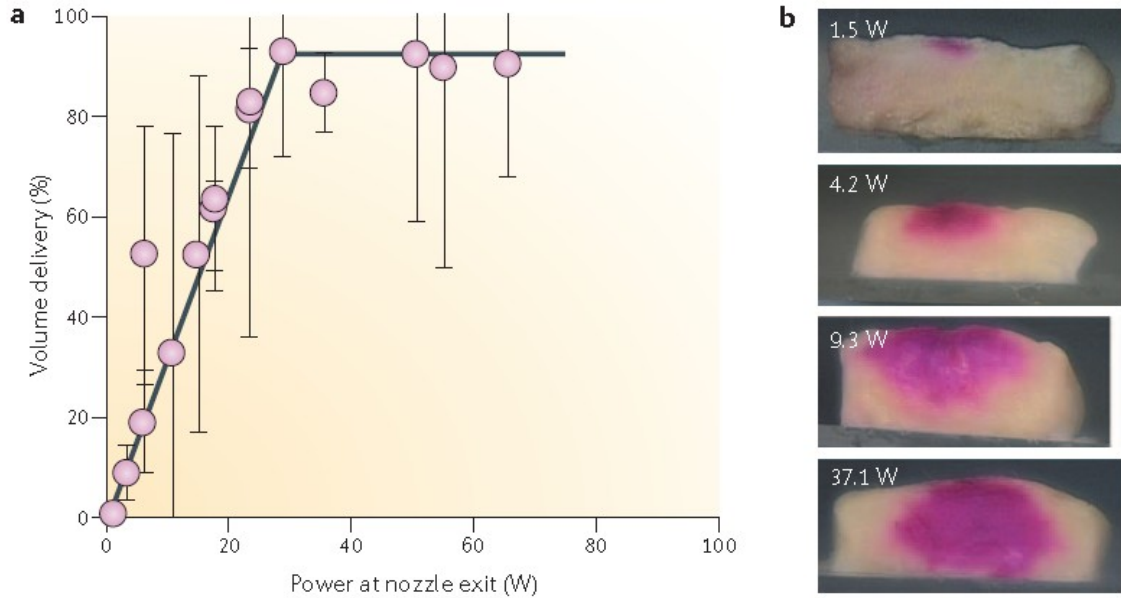


Figure 1.8. a) Delivery efficiency versus power; and b) penetration versus power (Mitragotri 2006)

Figure 1.8 depicts the relationship between volume delivery efficiency and nozzle power. This figure was produced using a constant nozzle diameter of 150 μm and injection volume of 80 μl (Mitragotri 2006). It is possible to conclude that higher power will indeed increase penetration depth as well as completeness of injections.

However, in the development of a needle free injector it will be necessary to deliver a complete injection at shallower depths, this will be required if new vaccines are to be used that target Langerhans cells in the epidermis. Consequently, it will be necessary to decouple the completeness of injection from the power required. In other words, choosing a lower power level for the jet should not compromise the completeness of injections. Current technologies are at the disposal of the medical field and engineering field in order to accomplish this goal and will be discussed later.

1.7. Liquid Jet Fluid Dynamics

The needle free liquid jet injectors are able to deliver drugs by creating small jets that have enough power to penetrate skin. The current commercially available needle free injectors are capable of producing jets that range from 76-360 μm and that travel at speeds in excess of 100 m/s. Literature shows that commercial injectors can produce an initial pressure change of 20,000 kPa within 0.5 ms. Consequently, with such great velocities and high pressures the resulting flow will inevitably be turbulent. The turbulent nature of the flow along with the micro nature of the jet makes modeling this behaviour very difficult to predict. In fact the mean Reynolds numbers for such jets are estimated to reach well above 100,000 (Mitragotri 2006). Nevertheless, studies demonstrate that these micro sized jets still exhibit traits observed on their larger counterparts. As the liquid jets exits the injector, the sudden decrease in pressure causes the under-expanded jet to fan out. Consequently, the jet emerging from the nozzle is slightly larger in diameter than the nozzle but still comparable in size. This also stresses the importance of stand-off distance, in order to maximize the jet pressure it is important to place the injector nozzle as close as possible to the skin. This pressure loss is caused by the dispersion of the jet in air. Once the jet penetrates the skin, it losses pressures quite rapidly, in fact the depth that the jet penetrates is established in less than a few milliseconds. As previously mentioned, the power loss is attributed to the jet entering a fluid filled region of the hole it pierced. Energy is absorbed by the fluid within the hole rather than being used to penetrate further into the skin.

Another important aspect governing the fluid dynamics of the jet that is emitted from the injector is the nozzle geometry and the path that the fluid takes to the nozzle exit.

Research has demonstrated that the nozzle geometries of various injectors are in the form of round holes. However studies have also been conducted in order to describe the resulting pressures and velocities of the liquid jet in relation to the pathway geometry of the fluid.

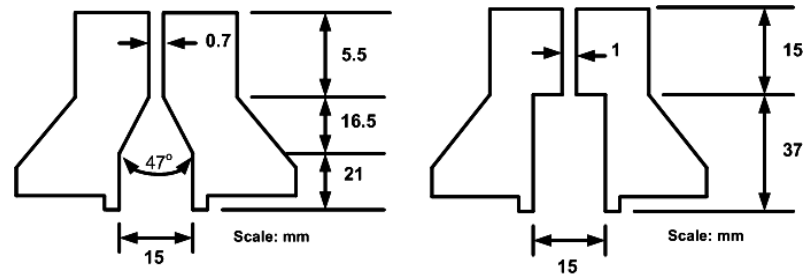


Figure 1.9. Geometries considered by Seehanam *et al.* (2009)

As is demonstrated in Fig. 1.9, the type of path the fluid can follow as it makes its way to the nozzle orifice can be numerous. Substantial work has been completed by Seehanam *et al.* (2009) on simulating impulse driven jets equivalent to those encountered in needle free liquid injectors. This study made it possible to numerically model the pressure and velocity profiles of the liquid jet emitted from the injector, beginning from the impulsive action of the piston which drives the fluid and then taking into account the pathway geometry in which the fluid follows. The study by Seehanam *et al.* analyzed two distinct shapes, one where the pathway converges in a cone like manner towards the final exit diameter, and the other where the path way abruptly changes diameter in a step-like manner. In order to model these two cases Seehanam *et al.* used Fluent[®], a commercially available CFD software; he also compared the results of his simulations with experimental results.

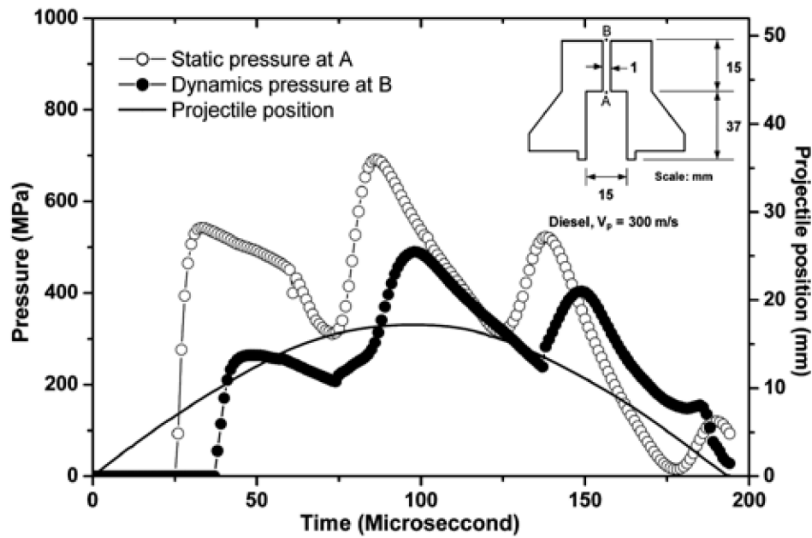


Figure 1.10. Pressure as a function of time for step-like geometry (Seehanam *et al.* 2009)

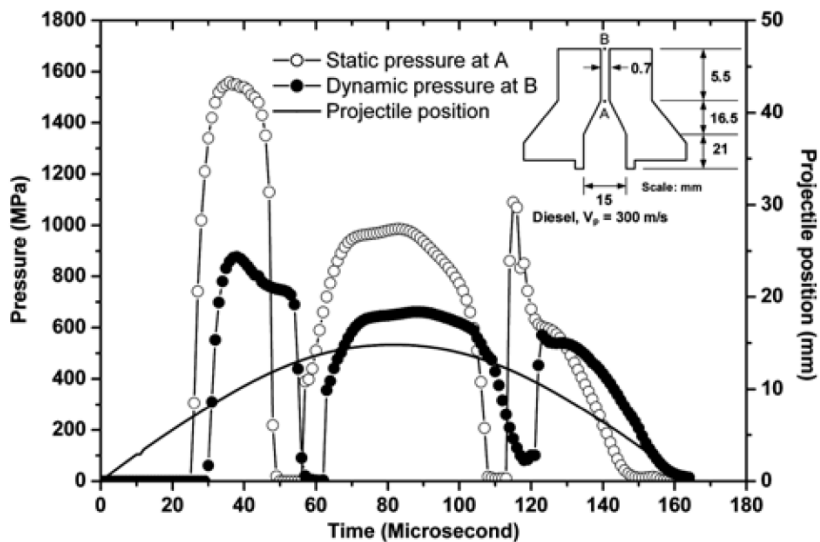


Figure 1.11. Pressure as a function of time for a conical geometry (Seehanam *et al.* 2009)

Figures 1.10 and 1.11 demonstrate the results of the pressure profile of the jet as a function of time, as well as piston position for both step-like geometry and conical geometry respectively. Comparing both cases it is possible to see that there are distinct differences for the pressure variations over time. Furthermore, it is also possible to

conclude that the conical nozzle produces a much higher pressure peak than the step-like geometry, in fact almost twice the pressure is produced. It is important to note that although Seehanam *et al.* (2009) did not use dimensions which represent the nozzle diameter and lengths found in typical needle free liquid injectors, it is possible to use his findings in order to improve the design and better understand the parameters which govern impulsive liquid jets. Figure 1.12 is a comparison of Seehanam's CFD results with experimental data. It is possible to observe a close correlation between the two. This study also mapped the jet velocity contours as it emerged into the atmosphere. However the working fluid for this part of the study was diesel, and the jet was mapped over a distance of 10 cm, consequently this does not clearly show the detailed velocity contours that arise in the first few millimetres of jet emergence.

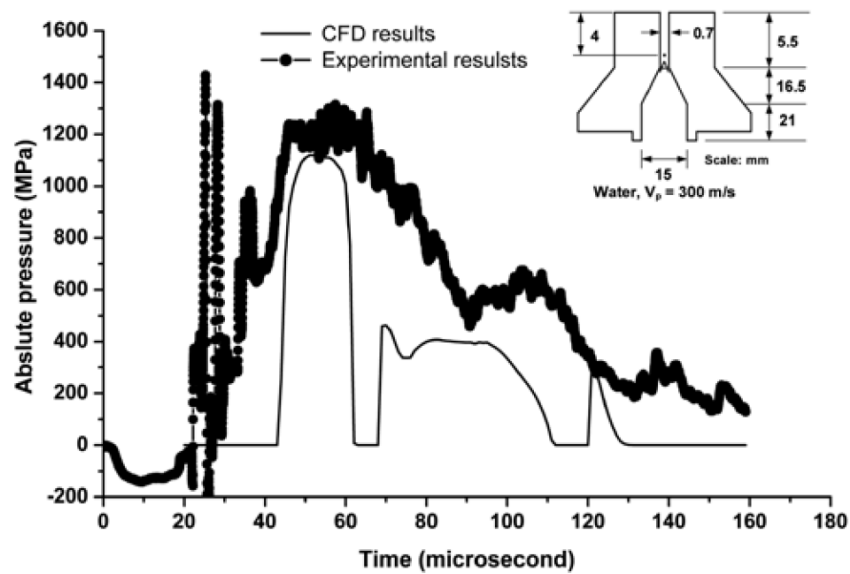


Figure 1.12. Comparison of experimental and theoretical results for nozzle pressure (Seehanam *et al.* 2009)

Although the impulse driven jets can be modeled using CFD software, there has also been some research in to solving the pressure and velocity distribution found within the

nozzle by analytical means. Baker and Sanders (1999) have conducted a continuum analysis whereby they assumed static incompressibility of the fluid, and neglected the effects of viscosity and turbulence. Their findings help characterize the sensitivity of injector design parameters such as piston area, as well as the pressure gradients that will be imposed on the drug to be injected. However it must be noted the study analyzed a spring powered injector, and thus his results cannot be extrapolated for an air-powered injectors.

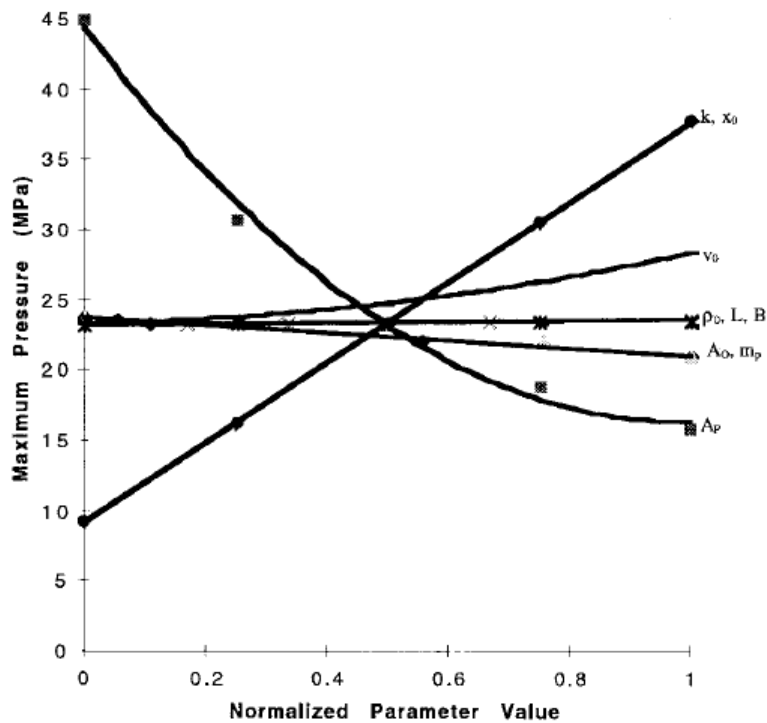


Figure 1.13. Maximum pressure as a function of parameter sensitivity by Baker and Sanders (1999)

Figures 1.13 and 1.14 represent the findings of Baker and Sanders (1999). These charts compare the effect of parameters such as: chamber length L , piston area A_p , initial piston velocity v_o , piston mass m_p , spring constant k , the initial density of the fluid ρ_o , the exit orifice cross sectional area A_o and the initial displacement of the piston x_o on the

maximum pressure that can be achieved as well as the time required to achieve this pressure. An efficient injector will produce the most possible pressure within the shortest time frame. Consequently, it is possible to conclude that in order to achieve maximum pressure in the fastest time a short chamber length, high initial velocity and large piston area are required. However it is important to note that the maximum pressure that can be achieved is also highly dependent on the piston area, a larger piston area will produce a short pressure rise time but will also reduce the maximum pressure of the injector. This is caused by the spring force being distributed over more surface area. Thus the efficient design of a needle free injector must be a compromise between many factors. The pioneering by Baker and Sanders (1999) provides a solid foundation on which to compare the sensitivities of various design parameters.

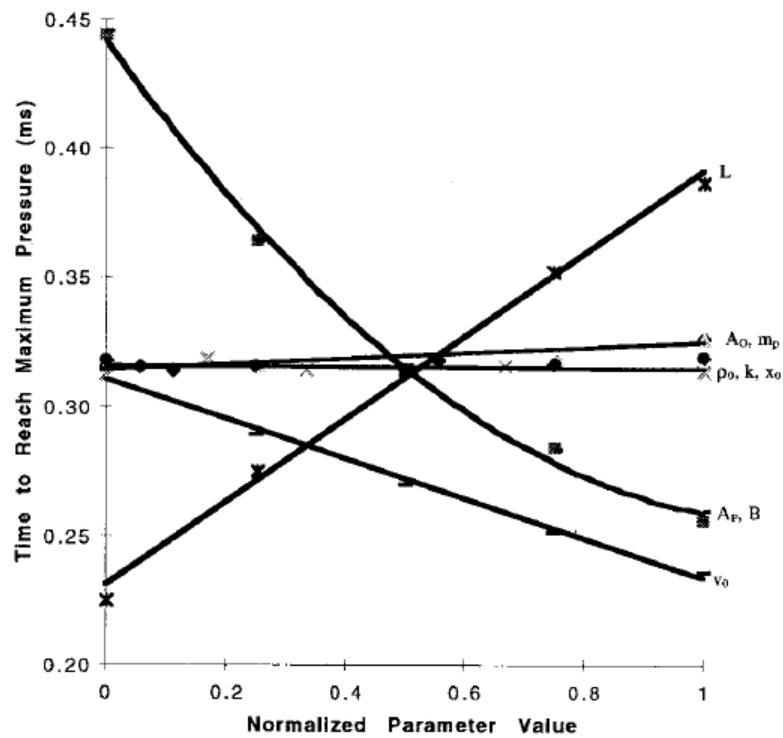


Figure 1.14. Time required for maximum pressure from parameter sensitivity by Baker and Sanders (1999)

Further enhancing the current knowledge of the fluid dynamics relating to jets penetrating human skin can help alleviate the problems associated with backslash which leads to cross contamination among patients. The current studies have only analyzed cylindrical style jets, perhaps with the advances in nanotechnology it will be possible experiment with different geometries of jets which might reduce the pressures and velocities needed in order to perforate the skin, as well as increase the completeness of injection. One such study conducted by Tagawa *et al.* (2012) utilizes only a 200 μm capillary tube filled with the medication to be delivered, and a low powered laser. The laser is used to heat air bubbles trapped within the capillary tube. The expansion of the air bubble and the subsequent rupture cause the fluid to be ejected as a very highly focused jet. Figure 1.15 illustrates the results of this study, and jets having a diameter as small as 10 microns can be produced via this technique.

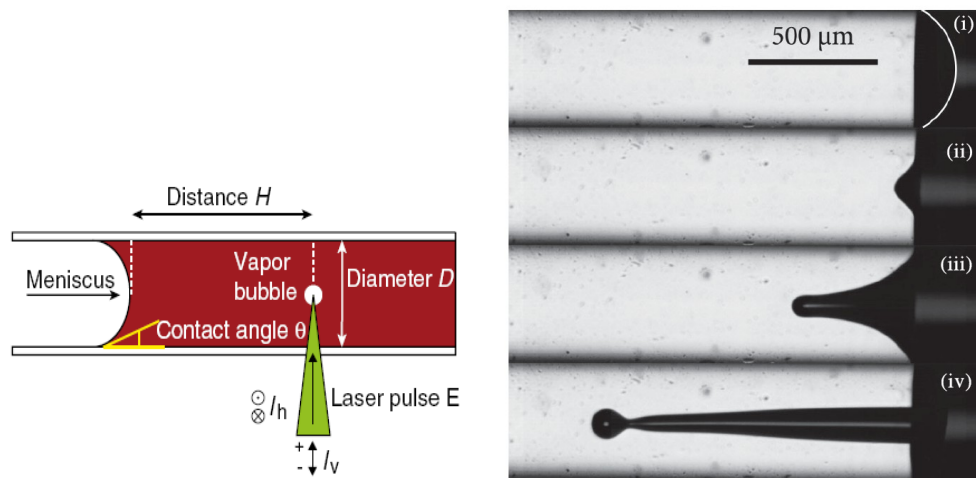


Figure 1.15. Production of highly focused jet (Tagawa *et al.* 2012)

1.8. Needle Free Liquid Jet Injector State-of-the-Art Technologies

Liquid jet injectors are perhaps the oldest form of needleless injection. The basic principles which govern the operation of liquid jet injectors is quite simple, a force is imparted on a cylinder which forces a column of fluid containing the drug through a nozzle, where it exits as a high speed jet, which penetrates the skin through a localized compression force. Studies have shown that commercially available injectors produce exit velocities greater than 100 m/s and diameters ranging from 100 to 360 μm . Typical delivery rates for commercially viable injectors range from 0.1 to 1 ml, with a penetration depth of up to 10 mm, at these depths it is possible to breach subcutaneous layers of the dermis and administer drugs to muscular tissues. Needle free liquid jet injectors are classified by their power source, some use a spring to activate the fluid, and others employ a disposal gas cartridge.



Figure 1.16. Typical layout of commercial injectors (Tev-Tropin Inc.)

Spring powered injectors utilize mechanical springs to store potential energy, which is then released when the injection is to be performed. In order to store the mechanical energy and deliver the injection the injector must undergo a priming procedure. This entails compressing the spring to a predetermined amount by means of a screw mechanism or a lever. Certain commercially available injectors that utilize the spring

technology require that the injector is cycled a few times in order to establish a good flow of fluid through the nozzle that is free of air. The spring within the injectors can be reused many times without replacement, in fact it can typically last the life of the injector. However, the spring powered injectors exhibit a wide variability of injection depths, due to the mechanical behaviour and inconsistencies of the spring mechanism. Furthermore, the priming procedure usually takes some time to complete, usually much longer than administering the injection, and some spring powered injectors require separate devices to prime the spring, which can be quite large and bulky. Consequently, this has led to an increase in the use of compressed gas as a power source (Baker and Sanders 1999).

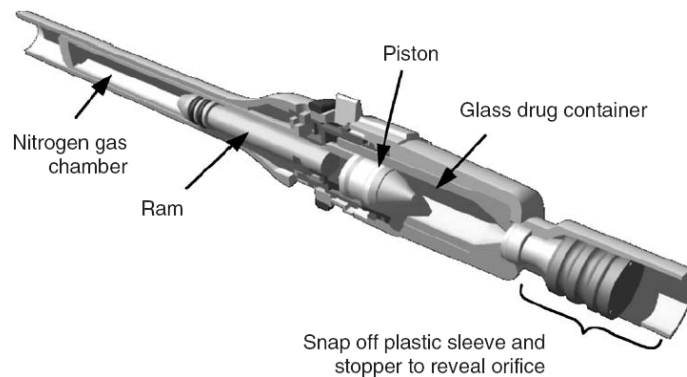


Figure 1.17. Schematic for gas powered injector (Shergold *et al.* 2005)

Gas powered needle free injectors utilize a disposable gas cartridge filled usually with CO₂. The gas cartridge is actuated by means of a valve mechanism which is usually triggered by a button on the injector body. The gas powered injectors can deliver much greater volumes of liquid than their spring powered counterparts. This is due to the fact that a gas powered injectors can maintain its injection pressure at a much higher levels for longer periods of time. A spring powered injector will exhibit a linear decrease in force over the injection time, due to Hooke's law, whereas the gas powered injector can

maintain a relatively constant injection pressure. This gives gas powered injectors the ability to penetrate deeper into the skin and deliver the larger quantities of medication. The major drawback with the use of the gas powered injectors is that the gas power source must be replenished. Depending on the volume of gas cartridge used, some injections can provide up to 10 to 15 injections. In order to overcome the limit of injections capable of being performed with one cartridge, manufacturers have also developed injectors that can be pressurized prior to performing injections. Again, these types of injectors require a priming procedure which can significantly increase the time required to perform an injection. Moreover, like their spring powered counter parts these self rechargeable injectors require large and bulky mechanisms in order to pressurize the injection chamber. Recently, manufacturers such as Biovalave, have been working on gas powered injectors, whereby the injector is pressurized through the reaction of several chemical components. The mixing of these components quickly produces large pressures, such as those observed in the deployment of air bags in the automotive industry (Mohanty *et al.* 2011).

Commercially available needle free injectors can be further subcategorized into two categories. They can be classified as Multi-Use Nozzle Jet Injectors (MUNJIs) and Disposable Cartridge Jet Injectors (DCJIs). As described by the name, the multi-use injectors can use the same nozzle tip, to deliver multiple injections. However these injectors were banned by the World Health and Safety Organization (WHO), because they exhibited a substantial ability to generate cross contamination between patients. It was observed that when the injections are administered there is some fluid backsplash on the nozzle, which in some cases contains bodily fluid from the patient. Consequently,

when the next patient is treated with the same nozzle this fluid can be transferred to his/her blood stream. As a result DCJIs are the only form of needleless liquid jet injectors approved by the WHO. DCJI injectors require that the injector tip that makes contact with human skin be replaced upon every injection. However because they consist of a onetime use cartridge which costs more to produce than a hypodermic needle, they have not seen widespread use (Kelly 2008).

Manufacturer	Type	Power Source
Algorx	Powder Injector	Helium
Antares	Liquid Injector	Spring
Aradigm	Liquid Injector	Carbon dioxide
Bioject	Liquid Injector	Spring/ Carbon dioxide
Biovalve	Liquid Injector	Chemical gas generation system
Careteck Medical	Powder Injector	Gas
CrossJect	Liquid Injector	Air bag gas generation system
National Medical Products	Liquid Injector	Carbon dioxide
Powder Med	Powder Injector	Gas
Visionary Medical	Liquid Injector	Gas

Table 1.2. Commercially available injectors and corresponding power source (Mohanty *et al.* 2011)

1.9. Objective of the present work

According to Table 1.2 gas/air powered needle free injectors have become very popular. However, evaluating various studies seems to indicate that there is a need to

further investigate the driving process for an air powered injector, as no clear model exists as of yet to accurately predict the behaviour of a high speed jet produced by these devices. Developing such a model would serve as a useful tool in the design and development of future air/gas powered injectors. Consequently this thesis will be devoted towards developing and validating a model to predict the characteristics of the liquid jet as it exits the injector, based on various injector parameters.

Chapter 2. Prototype and Physical Model

In this study a combined experimental and theoretical approach is used to investigate and assess the performance of air-powered needle-free injectors. It is important to create a validated prototype and develop a theoretical model to compare different results. This chapter is therefore devoted to the detailed design and development of the experimental prototype and the mathematical details of the theoretical model which will be used to analyze/investigate the phenomenon of this present study.

2.1. Prototype Design of the Injector

In order to improve the current status of needle free liquid jet injectors it is necessary to understand the relationships between the different engineering principles at play. This is accomplished by describing detailed models that govern the fluid interactions within the needle free injector as well as the interactions between the liquid jet and human tissue. It is also important to note that there exist a substantial number of commercially available liquid jet injectors that utilize different power sources and involve the use of complex mechanisms in order to function adequately. Modeling these mechanisms and comparing the differences in performance for several models would help determine which path should be pursued in order to build a more consistent and effective injector. Nevertheless, engineering data pertaining to these injectors is limited due to its proprietary and confidential nature. Consequently performing a study involving commercially available injectors will yield minimal results. In order to obtain a better understanding of the relationships governing the performance of needle free injectors it is

necessary to construct a prototype injector and subsequently perform a parametric study using this single device as a reference for comparison.

A prototype injector should be representative of the vast majority of commercially available injectors. This would entail utilizing a similar power source, propelling the medication in a similar fashion as well as maintaining consistent jet speeds and diameters. Once this objective is obtained, then a parametric study can be performed in order to verify the effect of variable parameters on injector performance. In this case prototype injectors was constructed by performing a detailed literature review on published data demonstrating the commonly used power sources, jet diameters and jet speeds. According to the data gathered in the previous chapter, the typical commercially available systems utilize a gas power source which consists of nitrogen or carbon dioxide filled cartridges. Furthermore it would seem that most commercially available injectors are capable of accelerating a volume of 0.5 ml or less to speeds of up to 200 m/s. Studies also show that jet stagnation pressures of 15 MPa are required to penetrate the skin.

The use of these standard values enabled the design of a prototype injector. The injector constructed for this experiment makes it possible to vary a number of parameters which are fixed on commercially available units. The pressure and nozzle diameter can be changed as well as the fluid volume. This makes it possible to verify the relationships between these parameters and the injector's effectiveness in delivering an injection. Figure 2.1 illustrates the design of the injector used throughout this study. In order to produce an injection it is first necessary to set the desired injection volume by adjusting the metering screw, this will determine the injection chamber length L . The injection chamber is then filled with the desired liquid and the nozzle is threaded on to the tip

sealing the chamber. The driver chamber can then be pressurized to a desired pressure. It is important to note that during pressurization the driver and the injection piston will not move. This is due to the design of the trigger mechanism, which consists of a partially threaded rod that links both the driver and the injection piston. The trigger block, locks on to the threads of the metering screw during pressurization, holding the entire injection assembly in place. Once the chamber is fully pressurized and the injection is to be administered the trigger handle is depressed, thereby disengaging the trigger block from the metering screw allowing both the driver and the injection piston to move forward and create a high speed jet.

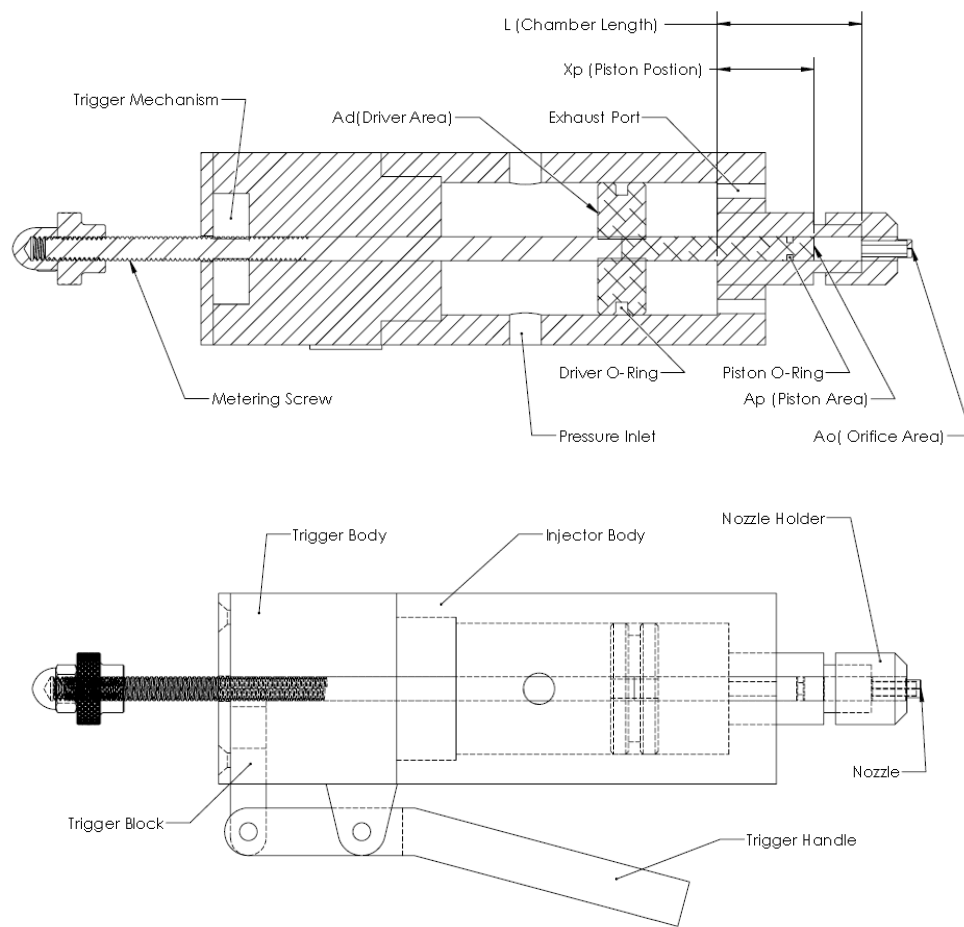


Figure 2.1. Schematic of prototype injector

The injector is able to create a high speed jet by utilizing the area ratio between the driver and the plunger. In order to size the prototypes so that it can simulate the behaviour of commercially available injectors, the stagnation pressure necessary to penetrate skin was first determined; studies demonstrate that this value ranges from 3 MPa to 15 MPa. Consequently, the injector was sized to be able to produce stagnation pressures up to 25 MPa on jet diameters of up to 200 μm . This was accomplished by computing the force required to produce the necessary pressure on the area of the plunger as well as determining the maximum pressure that can be obtained from readily available compressed air. Thus the driver pressure p_D and the jet stagnation pressure p_{ojet} make it possible to determine an area ratio between the driver A_D and the plunger A_p in order to produce the a high speed jet capable of penetrating human tissue. Although typical air powered injectors utilize nitrogen cartridges, they were not used during this study, due to the elevated quantity of injections to be performed. A compressor enables repeated charging of the injector, without the added cost of nitrogen filled cartridges.

$$\frac{A_D}{A_p} = \frac{P_{ojet}}{P_D} \quad \text{Eq. 2.1}$$

Using Eq. 2.1, it was possible to estimate the area ratio for the injector used in this study. The area of the plunger was predetermined due to machining limitations. Consequently, the plunger has a diameter of 6.35 mm, which yields a plunger area A_p of $3.166 \times 10^{-5} \text{ m}^2$, this implies that a maximum pressure of 20 MPa would result in a force of 650 N. The maximum pressure available to drive the injector measures 800 kPa, and it must produce a force greater than 650 N, thereby resulting in a driver are greater than $8.125 \times 10^{-4} \text{ m}^2$. The friction forces generated by the seals as well as the damping force of

the fluid also have to be considered, consequently, the area ratio was increased from 25 which results when no losses are considered to 30. Table 2.1 illustrates the important design characteristics of the injector.

Injector Parameters	
Nozzle Diameter	100 μm - 260 μm
Driver Pressure	3 Bar - 10 Bar
Injection Volume	0 ml - 1.2 ml
Piston Diameter	6.35 mm
Driver Diameter	38.1 mm
M_p (Mass of Piston-Driver Assembly)	80 g

Table 2.1. Prototype injector parameters

It is important to note that this analysis provides an approximate estimate to determine the approximate working dimension of the injector, given pressure and machining limitations. It is not a complete model of the injector and cannot be used to model the behaviour of the jet. However, it does make it possible to construct a prototype capable of penetrating skin as is illustrated by Fig. 2.2. The figure demonstrate the penetration capability of the jet at three different driver pressures, into bloom 250 ballistics gel that has been formulated at a 10% wt. ratio in order to mimic muscle tissue.



Figure 2.2. Penetration of prototype injector into polyacrylamide gel at a driver pressure of 700 kPa

The design of the prototype injector was performed by analyzing commercially available injectors and then conducting simple analysis to yield approximate working dimensions and pressures. However, in order to improve the current state of air powered injectors a model capable of predicting the stagnation pressure as well as the penetration depth of the jet is necessary. Creating such a model will make it possible to optimize the injector in relation to different design parameters. This will require a detailed analysis of the fluid motion, frictional forces and driving forces.

2.2. Model Describing Air-powered Injectors

In order to administer an injection using an air powered injector, fluid is compressed at high pressure and forced through a small orifice typically less than 200 μm in diameter. Consequently when fluid is compressed it provides a reaction force that serves to dampen the motion of the boundary forcing it through the orifice. If static incompressibility is assumed for the liquid behaviour then this dampening force can be found by determining the pressure of the fluid within the injection chamber at every instant of plunger displacement with respect to time. This can be achieved by performing a continuum

analysis on the liquid volume within the injection chamber. Baker and Sanders (1999) have conducted such an analysis on the fluid chamber used in spring powered injectors.

In order to model the injector in a similar fashion to that Baker and Sanders the injector was treated as a one-dimensional system whereby the fluid is assumed to be statically incompressible. This would imply that the mass flow rate through the injector is equal to the residual volume in the chamber and the in addition to the mass flow through the injector orifice:

$$\begin{aligned} &[\text{Initial Mass in Discharge Chamber}] \\ &= [\text{Residual Mass in Chamber}] + [\text{Mass Flow Through Orifice}] \end{aligned}$$

Using this relationship, it is possible to derive a relationship for the pressure generated in the liquid chamber. This model describes the pressure within the column of medication to be injected, by utilizing the bulk modulus of the liquid B , the initial density ρ_o , the piston area A_p , the exit orifice area A_o as well as the piston displacement X_p and fluid velocity u_o at the nozzle orifice. This model can then be used to in conjunction with a force analysis in order to yield the complete behaviour of the injector.

$$\rho_o A_p L = \rho A_p (L - X_p) + \rho_o A_o \int u_o dt \quad \text{Eq. 2.2}$$

$$\rho = \rho_o + \Delta\rho \quad \text{Eq. 2.3}$$

$$A_p L = \left(1 + \frac{\Delta\rho}{\rho_o}\right) A_p (L - X_p) + A_o \int u_o dt \quad \text{Eq. 2.4}$$

$$\frac{p}{B} = \frac{\Delta\rho}{\rho_o} \quad \text{Eq. 2.5}$$

Equation 2.6 illustrates the derivation for pressure; this considers the injector fluid chamber as a control volume and invokes the use of mass conservation whilst, relating the fraction of density increase from the initial density to the bulk modulus of the fluid and pressure.

$$A_p L = \left(1 + \frac{p}{B}\right) A_p (L - X_p) + A_o \int u_o dt \quad \text{Eq. 2.6}$$

$$pL - BX_p - pX_p + B \frac{A_o}{A_p} \int u_o dt = 0 \quad \text{Eq. 2.7}$$

$$L \frac{dp}{dt} - B \frac{dX_p}{dt} - X_p \frac{dp}{dt} - p \frac{dX_p}{dt} + B \frac{A_o}{A_p} u_o = 0 \quad \text{Eq. 2.8}$$

Equation 2.8 can then be obtained by simplifying and expanding Eq. 2.6 and differentiating variable terms with respect to time. Then it is possible to isolate for dp/dt and relate the fluid velocity u_o to pressure by using a simple Bernoulli stream line equation. It can be assumed that the fluid velocity at the piston $u_{fluid\ piston}$ is much less than at the nozzle orifice u_o consequently, it can be assumed that fluid velocity at the piston interface is zero.

$$\frac{\rho u_{fluid\ piston}^2}{2} + p_{piston} = \frac{\rho u_o^2}{2} + p_o \quad \text{Eq. 2.9}$$

$$p = p_{piston} - p_o \quad \text{Eq. 2.10}$$

$$u_o = \sqrt{\frac{2p}{\rho}} = \sqrt{\frac{2p}{\rho_o + \Delta\rho}} = \sqrt{\frac{2B\Delta\rho}{\rho_o^2}} = \sqrt{\frac{2p}{\rho_o}} \quad \text{Eq. 2.11}$$

Relating the fluid velocity at the orifice to the initial fluid density now makes it possible to yield an expression describing the pressure within the injector chamber based on parameters in Eq. 2.12.

$$\frac{dp}{dt} = \frac{(B + p) \frac{dx}{dt} - \frac{BA_o}{A_p} \sqrt{\frac{2p}{\rho_o}}}{L - X_p} \quad \text{Eq. 2.12}$$

This model has been experimentally verified for spring-powered injectors by Chen *et al.* (2011). In this study Chen *et al.* utilized a force probe in order to analyze the stagnation pressure of the jet as it exits the injector orifice. Figure 2.3 illustrates the experimental results obtained from this study, which compares stagnation pressure predicted from the model and experimental data.

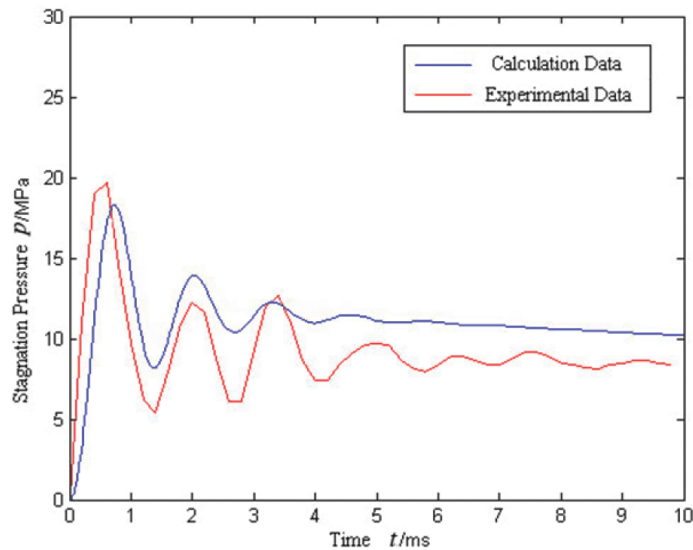


Figure 2.3. Experimental pressure trace for spring powered injector obtained by Chen *et al.* (2011)

Figure 2.4 illustrates the maximum stagnation pressure as a function of the injector spring rate. The experimental and theoretical results for this model match very closely.

Consequently it is possible to conclude that the model developed by Baker and Sanders (1999) can be successfully be invoked to predict stagnation pressure across of the injector jet as it exits into the atmosphere.

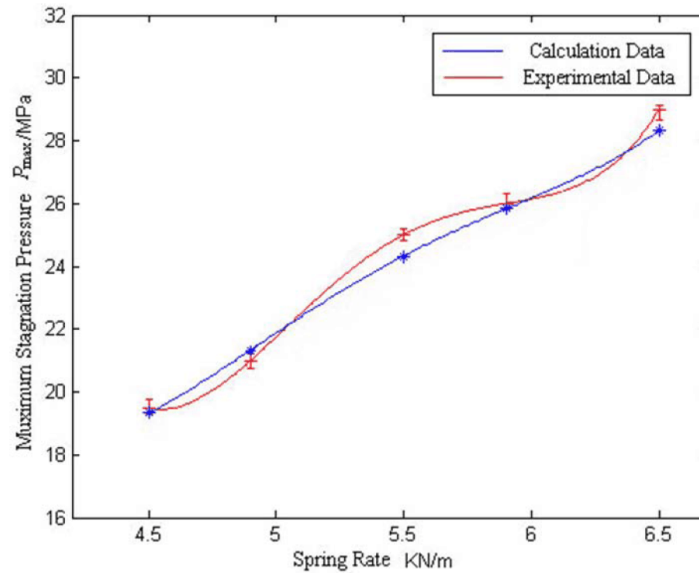


Figure 2.4. Spring rate as a function of maximum stagnation pressure obtained by Chen *et al.* (2011)

Past research has focused on the development of models which describe the stagnation pressure of spring powered injectors. However, most commercially available injectors are air powered and utilized compressed air as the driving force that delivers the injection. Consequently the model developed in this study will attempt to describe the jet stagnation pressure at the exit of the injector, by utilizing the model provided by Baker and Sanders (1999) and modifying the driving term in order to simulate the behaviour of air powered injectors.

2.3. Motion Analysis

In order to describe the complete time varying behaviour of the injector it is necessary to conduct a complete force analysis on the injector and develop equations of motion

describing the movement of the driver/plunger assembly. Having obtained the force invoked by the fluid as it is forced through the orifice, it is now possible to determine the behaviour of the driving force and those caused by friction.

2.4. Driving Force

The driving force which moves the plunger forward is produced by pressurizing the driver chamber. Figure 2.5 illustrates the geometry and variables within the driver chamber. The pressure within the chamber can be adequately modeled by using the ideal gas law. After the chamber is pressurized to a known pressure, the mass within the chamber can be easily computed. Once the initial mass of air m_a within the chamber is known, then the pressure within the chamber can be computed as a function of driver displacement.

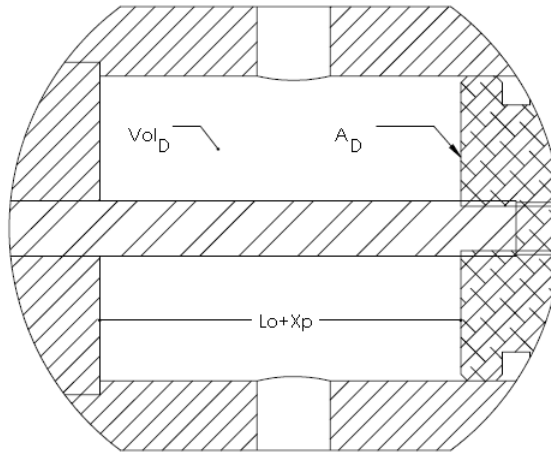


Figure 2.5. Driver chamber geometry

$$p_D = \frac{m_a RT}{Vol_D(t)} \quad \text{Eq. 2.13}$$

$$Vol_D(t) = (L_o + x_p(t))A_D \quad \text{Eq. 2.14}$$

2.5. Friction and Damping Forces

As the driving force begins to move the piston forward, there is resistance created by both O-ring seals as well as atmospheric pressure acting on the opposite side of the driver face. These forces must also be modeled in order to correctly simulate the injection process. Figure 2.6 illustrates a cross-section of the opposite side of the driver chamber, which is exposed to the atmosphere through two holes drilled from the front of the injectors. As the injection is administered the volume of this venting chamber is reduced causing the pressure to increase and thus damping the motion of the plunger as it travels. Consequently, the holes make it possible to vent the pressure build up in to the atmosphere as the injection progresses. It is important to note that the size of the holes is an important design consideration. If the holes do not maintain a certain area in relation to the mass flow rate through the secondary chamber, then the flow through the holes will be choked and the driver/plunger assembly will undergo damping. In order to ensure that the holes provide an adequate venting a detailed analysis was conducted. This analysis considered the volume change of the chamber with respect to time as well as the change in density of the air due to compression. The results of this analysis demonstrated that two holes of 4 mm in diameter would make it possible to not only avoid choking even at maximum piston speeds, but also to ensure that the same volume displacement by the piston will leave the driver chamber within the time of the piston movement so that no gas compression will occur. Nevertheless, the atmospheric pressure acting on the opposite face of the driver must be considered. This force can be assumed to remain constant throughout the injection process and is simply the product of atmospheric pressure and the driver area.

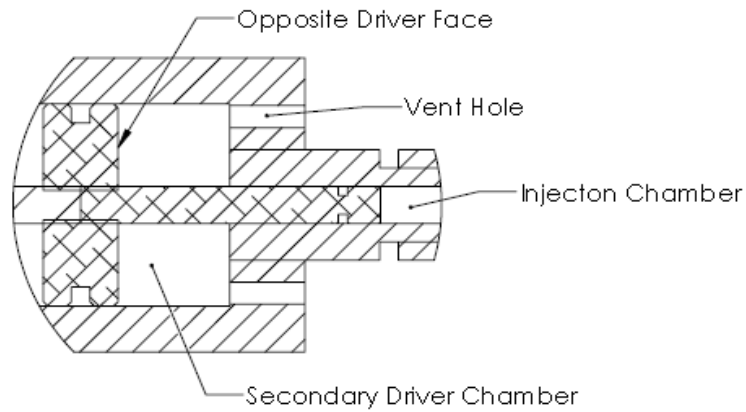


Figure 2.6. Cross-section of venting chamber

The frictional forces within the mechanism serve to counteract and damp the movement of the driver/piston assembly. The friction is caused by the O-ring seals which make contact and rub against the inner walls of both the driver chamber and the injection chamber. It is important to note that predicting the exact force imposed by O-ring friction is a very difficult undertaking. There exist many variables that must be considered such as the type of O-ring material, the fit and finish of the surfaces in contact as well as the pressure gradients across the seal. Complicating matters, is the fact that the movement of driver/plunger assembly requires the use of a reciprocating style seal. The friction forces generated by this type of seal are highly variable and depend on the not only the pressure gradient across the seal but the velocity that the seal rubs against the sealing surface. Consequently, in modeling the o-ring friction forces some assumptions must be made in order to make the computation of these forces feasible in a one-dimensional model.

In order to model the O-ring friction it must be broken down into two components, the first consists of the friction force caused by the compression fit of the O-ring into its housing, the second force is a result of the thin fluid film which is generated in the

clearance gap between the two components that the O-ring must seal. The forces caused by the compression of the O-ring, in the barrel of the injector is also dependent on the force generated by the pressure of the fluid. Consequently, the two major forces causing O-ring friction must be coupled in order to accurately model friction.

In order to model friction it is first necessary to compute the force imposed by a thin fluid layer on the O-ring seal. A similar approach adopted by Chen *et al.* (2011) was used. This process begins by determining the volumetric flow rate through the small clearance gap between the plunger and outer barrel of the injector. Figure 2.7 illustrates that this flow rate is equivalent to the product of velocity of the fluid across the gap multiplied by the corresponding cross-sectional area. Consequently, the flow rate can be found by integrating the velocity profile as a function of an infinitesimal change in gap height. This relation is expressed by the Eq. 2.15.

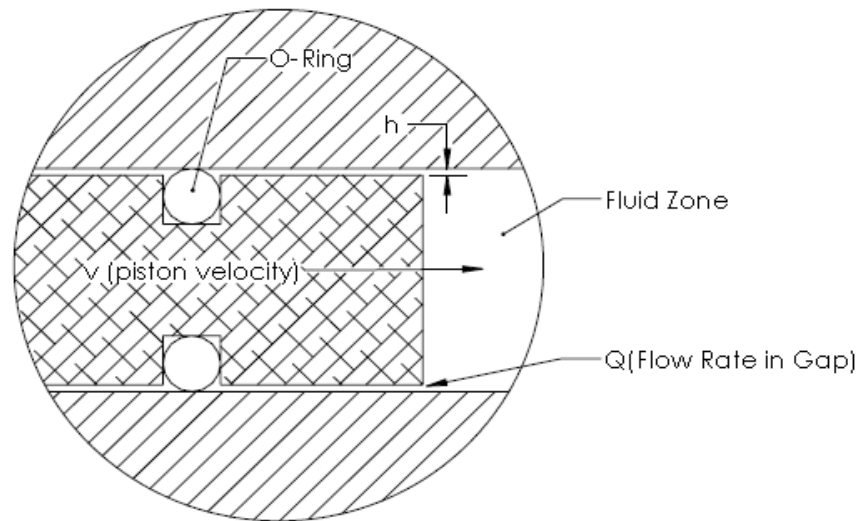


Figure 2.7. O-ring friction parameters

$$\frac{Q(t)}{\pi D} = \int_0^h v(t) dy = \bar{v}(t) h_c \quad \text{Eq. 2.15}$$

$$\frac{Q(t)}{\pi D} = \frac{1}{2} U_p(t) h_c \quad \text{Eq. 2.16}$$

$$h_c = \frac{2Q(t)}{\pi D U_p(t)} \quad \text{Eq. 2.17}$$

From Eq. 2.16 it is now possible to express the maximum film thickness as a function of volumetric flow rate. It is then possible to invoke the classical Reynolds equation which is commonly used in tribology to determine the pressure in thin films as derived by Sneek and Vohr (1983). The full Reynolds equation is given below and then simplified for this specific case. It is derived by solving the continuity equation and Navier-Stokes equations simultaneously. However, due to the special properties of thin fluid films there are a few critical assumptions that must be made before doing so. Due to the thin nature of the film inertial forces and body force can be considered negligible. Furthermore, the thin nature of the film implies that the pressure variation across the thickness of the film is negligible. Lastly, the working fluids in this model are treated as incompressible. The fluid administered through the injection chamber consists of water, and as such can be considered incompressible for the purpose of friction analysis. Moreover, although the working fluid in the driver chamber is a gas, the piston movement will likely never attain a speed in excess of 10 m/s, consequently the gas can also be treated as an incompressible fluid. Using these assumptions it is now possible to simplify the Navier-Stokes and solve them to lead to the Reynolds equation.

$$\frac{\partial p_r}{\partial x} = \mu \frac{\partial^2 u}{\partial y^2} \quad \text{Eq. 2.18}$$

$$\frac{\partial p_r}{\partial z} = \mu \frac{\partial^2 w}{\partial y^2} \quad \text{Eq. 2.19}$$

$$\frac{\partial u}{\partial x} + \frac{\partial v}{\partial y} + \frac{\partial w}{\partial z} = 0 \quad \text{Eq. 2.20}$$

Equations 2.18 and 2.19 can then be integrated twice with respect to y and using the boundary conditions that the fluid velocity at $U(0) = U_1$, $W(0) = 0$ and $U(h) = U_2$, $W(h) = 0$. The result of this integration is illustrated in Eqs. 2.21 - 2.22:

$$u = \frac{1}{2\mu} \frac{\partial p_r}{\partial x} (y^2 - yh) + \left(1 - \frac{y}{h}\right) U_1 + \left(\frac{y}{h}\right) U_2 \quad \text{Eq. 2.21}$$

$$w = \frac{1}{2\mu} \frac{\partial p_r}{\partial z} (y^2 - yh) \quad \text{Eq. 2.22}$$

If both $\partial u/\partial x$ and $\partial w/\partial z$ are integrated with respect to y using the limits that $y(0) = 0$ and $y(h) = h$ and the results of this integration are then substituted into the continuity equation, it is then possible to obtain a generalized formula of the Reynolds equation given in Eq. 2.23. For simplicity it is also possible to group together $U = U_1 - U_2 = U_p$ which will relate to the speed of the boundary pushing the fluid.

$$\frac{\partial}{\partial x} \left(\frac{h^3}{\mu} \frac{dp_r}{dx} \right) + \frac{\partial}{\partial z} \left(\frac{h^3}{\mu} \frac{dp_r}{dz} \right) = 6(U) \frac{\partial h}{\partial x} + 12 \frac{\partial h}{\partial t} \quad \text{Eq. 2.23}$$

For the case of the fluid pressure on the O-ring seal it can be assumed that the pressure gradient in the y direction is negligible due to the small thickness in this

direction compared to that in the x direction. Therefore the generalized equation can be further simplified by denoting only the variation in the x direction.

$$\frac{\partial}{\partial x} \left(\frac{h^3}{\mu} \frac{dp_r}{dx} \right) = 6(U) \frac{\partial h}{\partial x} \quad \text{Eq. 2.24}$$

$$\left(\frac{h^3}{\mu} \frac{dp_r}{dx} \right) = 6(U)h + C \quad \text{Eq. 2.25}$$

If it is assumed that at maximum fluid film pressure $dp_r/dx = 0$ and at this point $h = h_c$ then it is possible to integrate the above equation to determine the pressure distribution across the face of the O-ring seal, i.e.,

$$\left(\frac{dp_r}{dx} \right) = 6\mu(U(t)) \frac{h - h_c}{h^3} \quad \text{Eq. 2.26}$$

In the case of the injector, it is known that h_c is an average value that depends on the volumetric flow rate through the clearance gap that the O-ring seals. Consequently, it is known that if the seal does not leak there is no flow through this area, and $h_c = 0$.

$$\left(\frac{dp_r}{dx} \right) = \frac{6\mu(U(t))}{h^2} \quad \text{Eq. 2.27}$$

This equation can now be integrated with respect to x and the pressure distribution on the O-ring seal can easily be computed. Equation 2.28 represents the complete fluid pressure imposed on the O-ring seal in the direction of fluid flow, the variable h in this equation represents the film thickness at a wedge shaped inlet determined by the O-ring

and housing dimensions, according to Fig. 2.8 this dimension is equivalent to the clearance gap.

$$\bar{p}_{O-ring} \approx \frac{1}{2} \frac{6\mu U(t)}{h^2} \frac{d}{2} + p(t) \quad \text{Eq. 2.28}$$

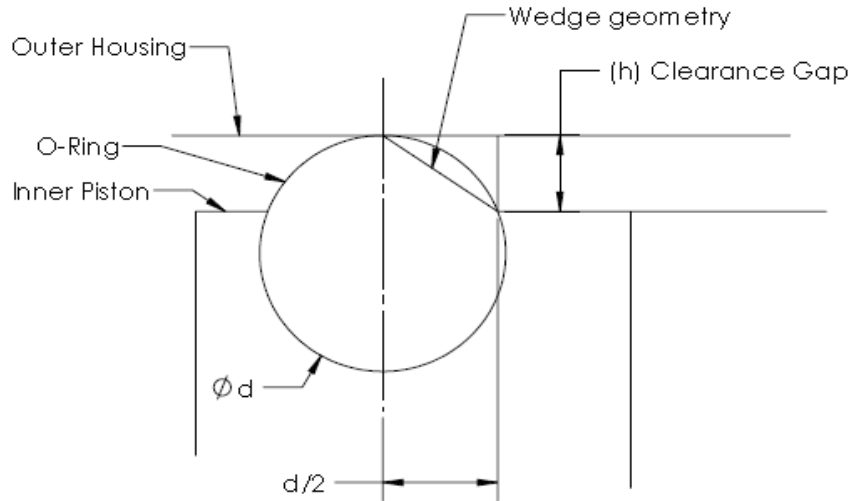


Figure 2.8. O-ring wedge geometry

As a result of knowing the pressure imposed by the fluid on the O-ring seal the resisting force caused by this pressure is simply the area of exposed O-ring multiplied by the corresponding pressure, i.e.,

$$F_{fluid} = \bar{p}_{O-ring} \pi D h \quad \text{Eq. 2.29}$$

The second component of the frictional forces consists of the friction force caused by the compression of the O-ring due to its press fit into the barrel of the injector chamber as well as the compression caused by the pressure exerted by the fluid. In order to determine the force caused by the press fit into the barrel it is possible to invoke the use of empirical charts detailing the amount of compression fit as a function of load that an O-ring will

produce. Figure 2.9 depicts the relationship between the forces imposed by the O-ring on the outer barrel wall as a function of O-ring compression, for different durometer, 0.070” (1.78 mm) cross-section O-rings.

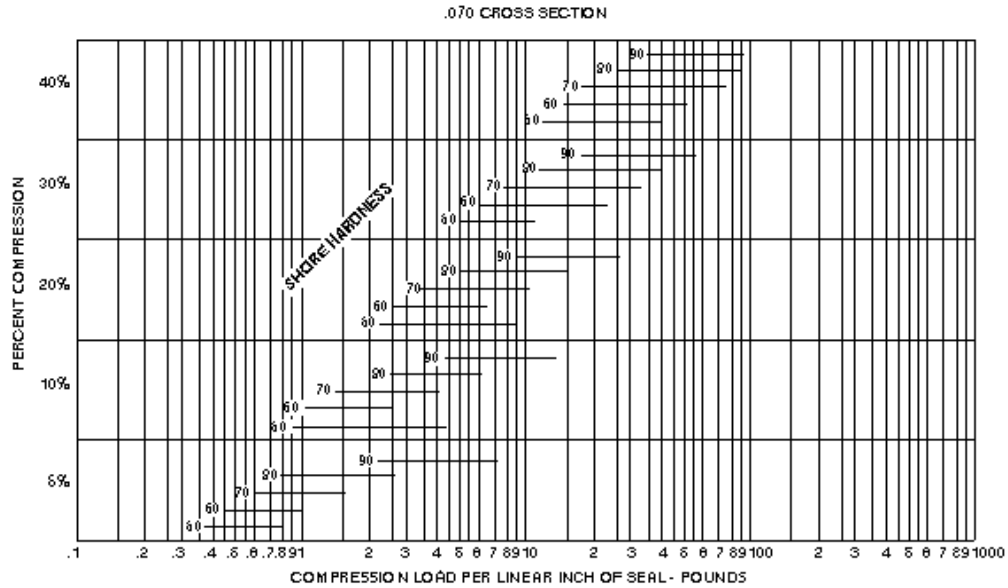


Figure 2.9. O-ring load per linear in of seal as a function of compression fit (Darcoid 2013)

The grooves containing the O-rings with the injector were manufactured to impose a compression of 5%; consequently it is possible to use the empirical charts to estimate the amount of compression that is provided by the O-ring fit. Table 2.2 illustrates the three different size O-rings within the injector as well as the corresponding amount of load they produce for the given clearance.

Compression Load Produced by O-rings						
%Compression	Material	Cross-section (in)	Size O.D. (in)	Durometer	Load per Linear Inch	Complete Load (N) f_c
5	Nitrile	.070	.250	70	1	3.49
5	Nitrile	.070	.375	70	1	5.24
5	Nitrile	.139	1.375	70	5	96.10

Table 2.2. Compression load produced by O-rings within injector body

In addition to the force caused by the compression of the O-ring into the barrel of the injector, it is also necessary to take into consideration the transfer of forces caused by the fluid pressure on the O-ring. The fluid pressure that acts on the seal also serves to further increase the compression loading. Studies conducted by Guang and Wang (1994) demonstrate that the transfer coefficient between the fluid pressure acting on a seal in relation to the increase of compression force of the O-ring can be estimated at 1. In other words, the pressure contained within the thin film acting on the seal almost entirely serves to increase the amount of compression forces on the sealing surfaces. Consequently, having completely described the force action upon the O-ring seals and knowing that the coefficient of friction between aluminum and nitrile rubber is 0.2, it is possible to fully describe the resisting force encountered by individual O-ring seals in the injector through Eq. 2.30.

$$f_{O-ring} = 0.2((\bar{p}_{O-ring}(t))\pi Db + f_c) + (\bar{p}_{O-ring}(t))\pi Dh \quad \text{Eq. 2.30}$$

Where b in Eq. 2.30 corresponds to the contact patch due to O- ring compression and is obtained experimentally.

2.6. The Complete Model

Using the results of each individual analysis on the different section of the injector, it is possible to create a model capable of predicting the jet stagnation pressure as a function of time. This complete model considers all forces acting on the injector with respect to time.

$$\frac{dp}{dt} = \frac{(B + p)\frac{dx}{dt} - \frac{BA_o}{A_p} \sqrt{\frac{2p}{\rho_o}}}{L - X_p} \quad \text{Eq. 2.12}$$

$$\frac{d^2x}{dt^2} = \frac{A_D \left(\frac{m_a RT}{Vol_D(t)} - P_{atm} \right)}{M} - \frac{A_p p(t)}{M} - \frac{(f_{O-ring1}(t) + f_{O-ring2}(t) + f_{O-ring3}(t))}{M \left| \frac{dx}{dt} \right|} \frac{dx}{dt} \quad \text{Eq. 2.31}$$

Solving Eqs. 2.12 and 2.31 simultaneously makes it possible to determine the driver/piston displacement, velocity as well as jet stagnation pressure. This is accomplished by means of numerical integration using a Runge-Kutta 4th order scheme. The two equations are decomposed into three first-order ODEs and then solved by writing a Matlab script.

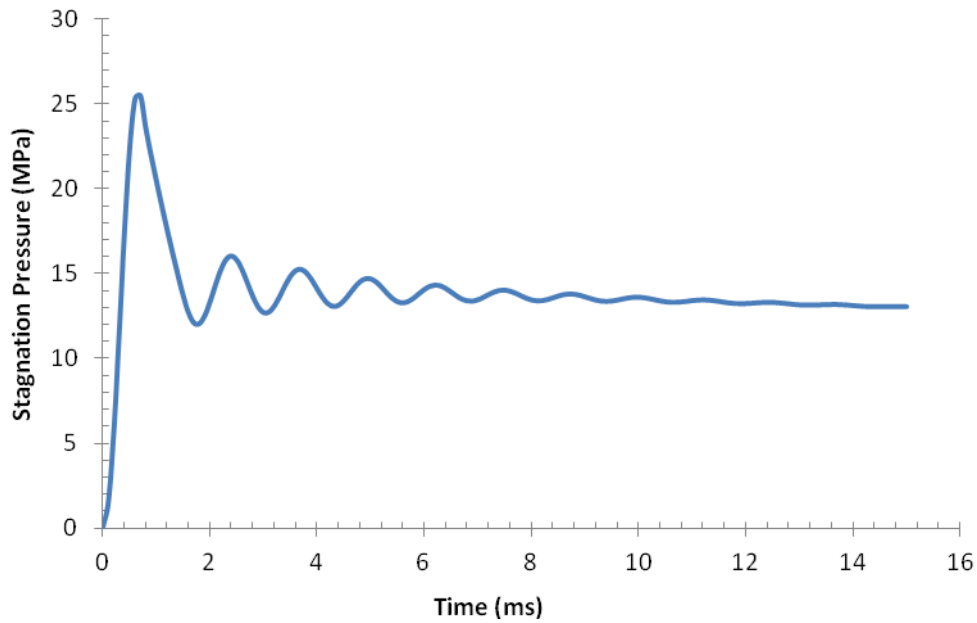


Figure 2.10. Numerical simulation of jet stagnation pressure

Figure 2.10 above illustrates the preliminary behaviour of the model for the variation of stagnation pressure as a function of initial injection time. It is important to note that the injection attains a peak pressure very early on in the injection process, usually within the first few milliseconds; the pressure immediately stabilizes to an average value. It is these first few moments of the injection which are critical in determining the depth that the

injection will have as well as its subsequent ability to deliver the target amount of volume to the injection site. The stagnation pressure can then be further converted to jet speed as it exits the orifices. If it is assumed that viscous losses are negligible, across the orifice, then it is possible to invoke a simple Bernoulli equation to acquire jet speed from stagnation pressure.

$$V = \sqrt{\frac{2p}{\rho}} \quad \text{Eq. 2.32}$$

Figure 2.11 depicts the above relation; it is possible to observe that using standard injection parameters such as 8 bar driver pressure and a 200 μm nozzle has yielded realistic jet velocities. The jet velocity peaks at 250 m/s and then averages to 160 m/s, this is in accordance with results from past studies, which describe necessary jet velocities to obtain skin penetration. Consequently, this preliminary analysis of the model serves to validate the injector design parameters for its use in conducting a parametric study on the aforementioned model.

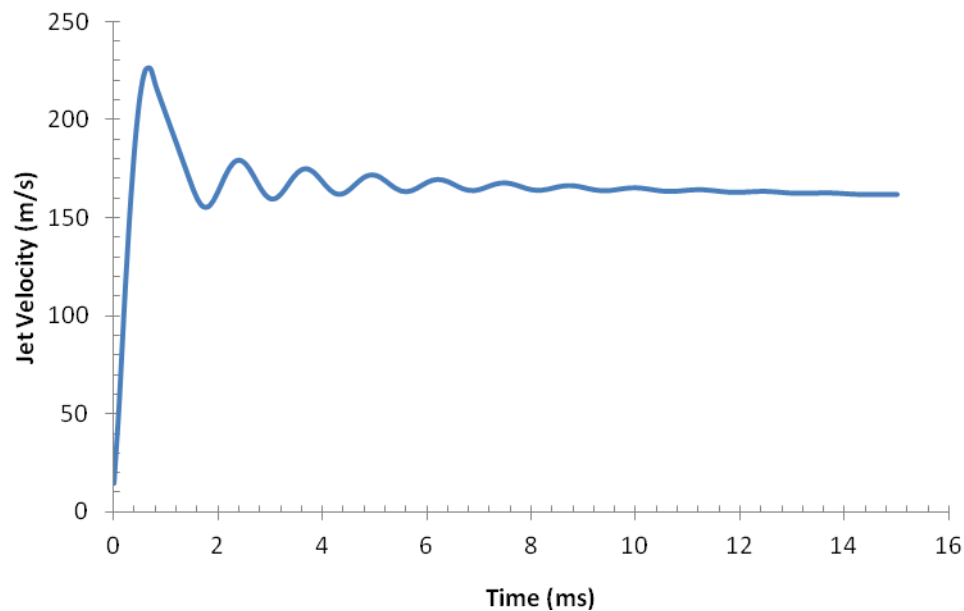


Figure 2.11. Numerical simulation of jet velocity

It is also possible to track the piston/driver velocity and displacement as a function of time. Figure 2.12 illustrates this behaviour. As is expected the maximum piston velocity occurs at the very beginning before the frictional forces and fluid forces can damp the motion. It is also important to note that the jet velocity predicted by the model and the piston velocity vary by two orders of magnitude. This can be explained if the piston movement is analyzed in terms of acceleration. The change in piston velocity over a tenth of a millisecond at the initial stages of injection represents an acceleration of 4500 m/s^2 , which falls to a value under 1 m/s immediately after this peak.

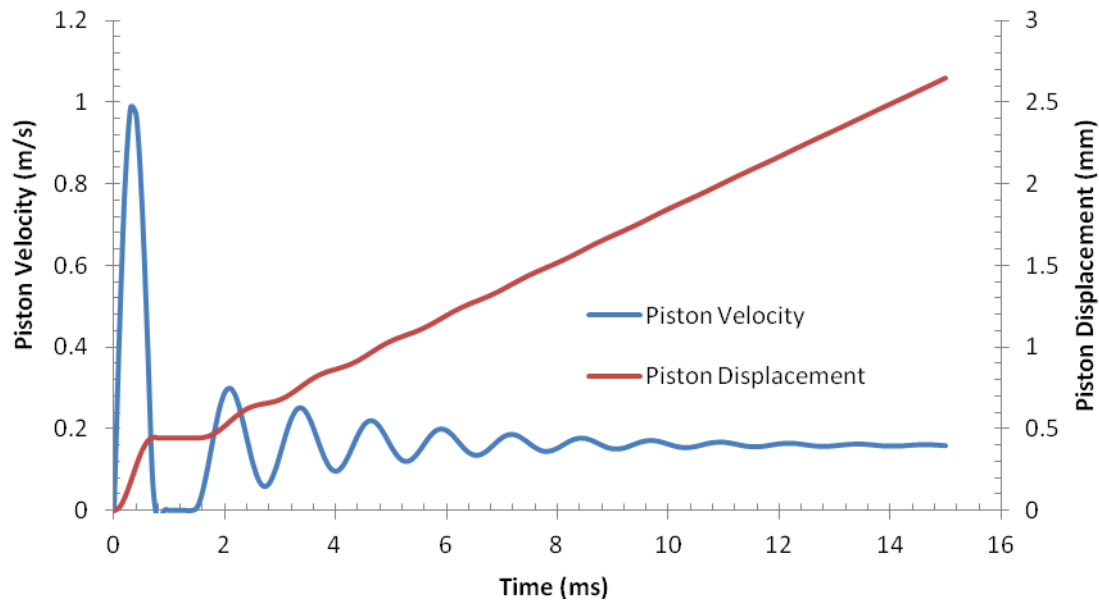


Figure 2.12. Numerical simulation of driver/piston velocity and displacement

The analysis performed in this chapter has made it possible to construct a simple one-dimensional model capable of predicting the stagnation pressure and velocity of the liquid jet based upon an initial driver pressure. This model can now be used to verify the effects of different injector parameters such as nozzle orifice diameter, driver pressure,

injection chamber length as well as the effects of mechanical friction on injector performance. Nevertheless, the model must first be experimentally verified in order to establish its usefulness in predicting injector behaviour.

Chapter 3. Results and Discussion

The experimental approach used in this study consists of two distinct parts, the first entailed performing a qualitative assessment on the newly designed injector. This was done in order to validate the basic mechanism and verify that the injector output is indeed representative of the vast majority of commercially available air/gas powered units. The second part consisted of a quantitative assessment of the injector as well as the one-dimensional model. This involved measuring the stagnation pressure of the liquid jet as it exits the injector and then comparing it with theoretical results. Furthermore several parameters were varied during the experimentation in order to observe the effect of these parameters on injector performance and validate model predictions.

3.1. Qualitative Assessment

In order to validate the model describing the behaviour of air powered injectors it was necessary to subject the prototype injector to qualitative performance tests. This was accomplished by evaluating the ability of the injector to penetrate human tissue and using high speed photography to gain insight on the jet behaviour. After constructing the preliminary prototype, it was necessary to verify if it was possible to penetrate human tissue. This was accomplished by performing injections on two different media. The first consists of ballistics gel which has a bloom number of 250, and the second consists of actual animal tissue. Figure 3.1 illustrates a typical profile of for an injection administered into 0.75" thick gel. The penetration was visualized by using a blue die mixed with water; the depth of the injection can then be noted by measuring the length of

the blue column. It is important to note that although ballistics gel makes it possible to match the mechanical properties of skin, it does not have the same porosity.

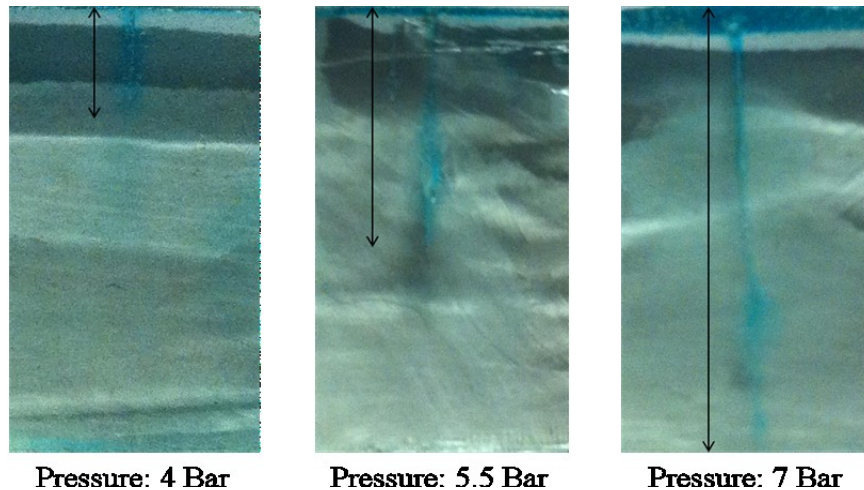


Figure 3.1. Penetration into bloom 250 ballistics gel with 200 μm nozzle

Consequently, the actual geometry at the end of the column cannot be compared to that generated in human tissue. In order to verify that the injector delivers medication in a similar fashion to commercially available units, animal tissue was used. Figure 3.2 depicts an injection delivered on a piece of 0.75" bovine meat, the injector clearly punctures the skin and delivers the medication in a similar bulb formation to that of commercially available injectors.



Figure 3.2. Cross-section of penetration test on 20 mm thick bovine meat with 200 μm nozzle and 0.1 ml injection volume

There were several tests conducted on ballistics gel in order to establish a general trend for penetration as a function of nozzle size and driver pressure. Figure 3.3 demonstrates that as the nozzle size as well as the driver pressure is increased, the penetration depth seems to increase linearly as well.

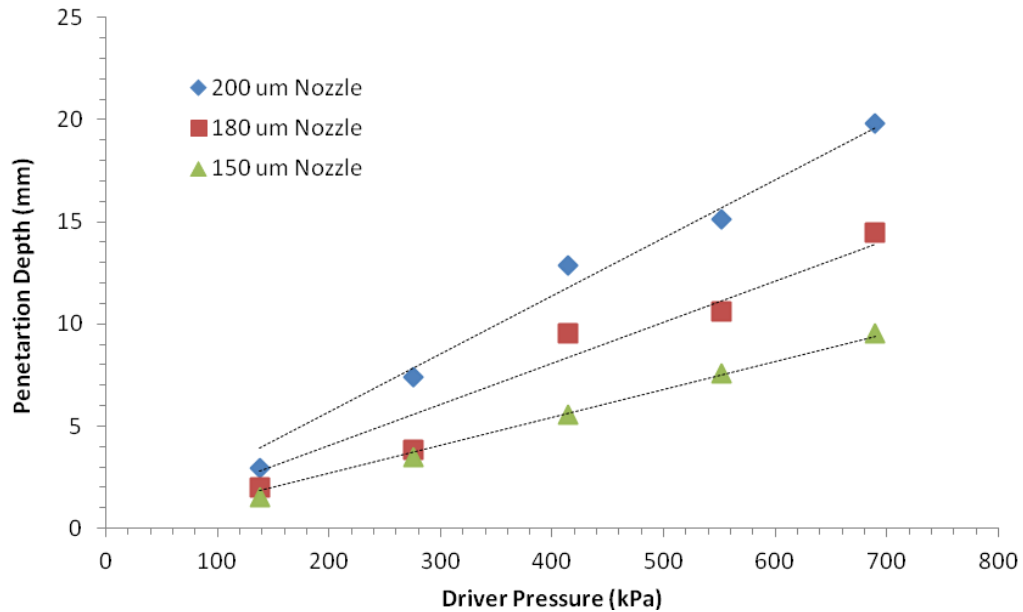


Figure 3.3. Penetration depth into bloom 250 10% wt. gel as a function of driver pressure

In order to further verify the performance of the prototype injector, it was necessary to observe the behaviour of the jet as it exits into the atmosphere. This was accomplished using a high speed camera (PCO.1200hs). Figure 3.4 is a sample of jet behaviour, the jet is photographed as it emerges from a 180 micron diameter nozzle powered at 689 kPa, and the jet speed is computed using the inter-frame time step (0.035 ms). The images demonstrate that the jet speed is within the same range exhibited by commercially available units. Furthermore, the photographs also provide a clear depiction of jet divergence. As the jet emerges into the atmosphere it fans out and diverges from its initial

180 micron diameter. It is important to note that although the jet diverges dramatically in the atmosphere, it remains confined when penetrating various medium.

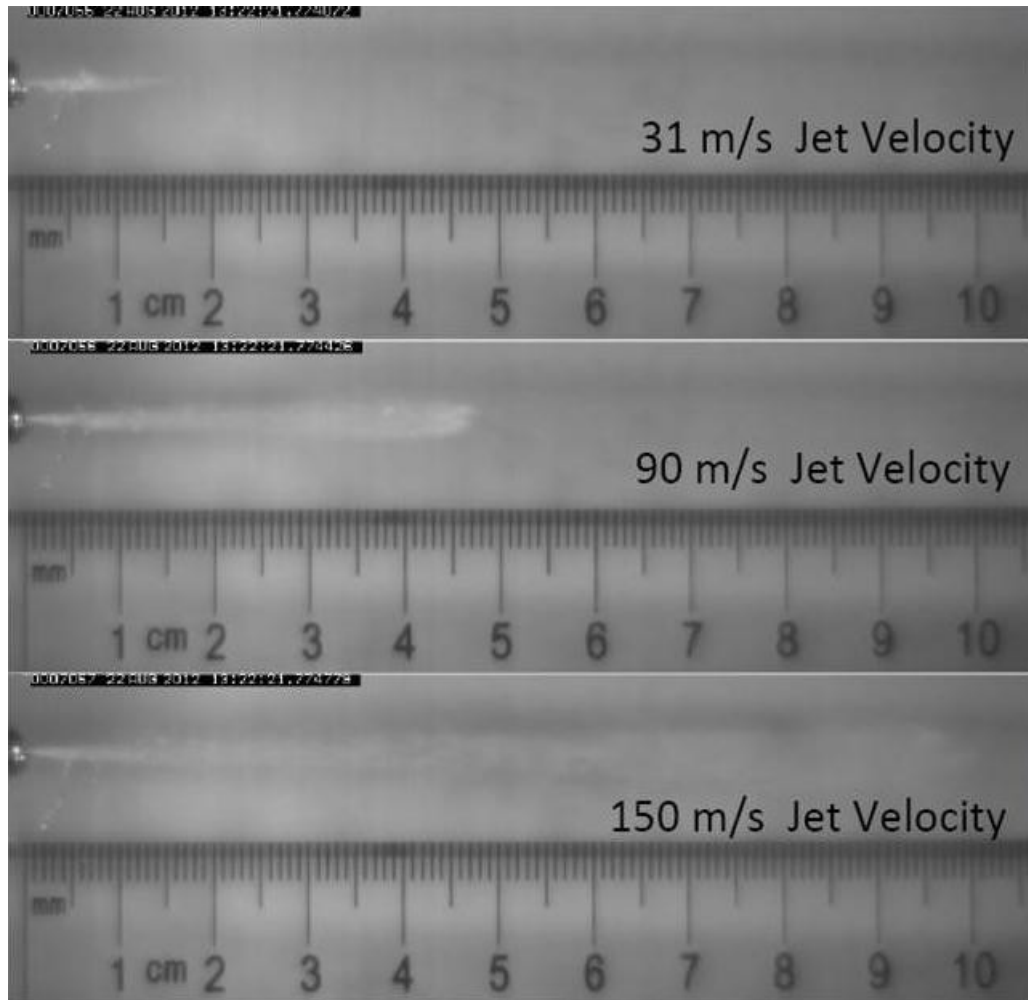


Figure 3.4. High speed photography of liquid jet with 180 μm nozzle and at 700 kPa driver pressure

The high speed photography of the liquid jet was also compared with a numerical simulation that utilizes the same injector geometry and parameters. In this comparison, simulations of the high speed liquid jet generation process from the needle-free injector are carried out using the Open FOAM[®] CFD software package (OpenCFD 2009). Figure 3.5 illustrates the results of a jet produced with a 180 μm nozzle at a driver pressure of

700 kPa. These results were produced by Nakayama *et al.* (2013), and model the exact geometry of the injector presented in this study. The dynamic behavior of the liquid jet is approximated using a multi-phase compressible, isothermal immiscible fluids LES solver and the VOF method for the interface capturing, available in OpenFOAM®. The liquid jet is generated by dynamic mesh techniques, i.e., the liquid retained in the injector chamber is impacted by a moving boundary used to simulate the injector piston displacement driven by the driver air pressure. The driver/plunger velocity profile is provided by using the results of the model presented in Chapter 2. The results of this simulation seem to match very closely with the experimental photos. The amount of divergence of the jet is on the same order of magnitude as the simulation, moreover the numerical simulation makes it possible to have a clear understanding of the initial jet shape as it exits into the atmosphere, this is difficult visualize with the current high speed camera as the phenomenon occurs extremely quickly and even with an inter-frame time of 0.35 ms, only three frames can be obtained from the appearance of the jet into the atmosphere to final point in the viewing area of the camera. Consequently, by obtaining a numerical simulation describing exit of the jet into the atmosphere, it is possible to conclude that at the initial stages the jet divergence is minimal. This will play an integral role in the computation of the stagnation pressure as the jet force of the jet can then be assumed to be spread over approximately the same area of the nozzle orifice.

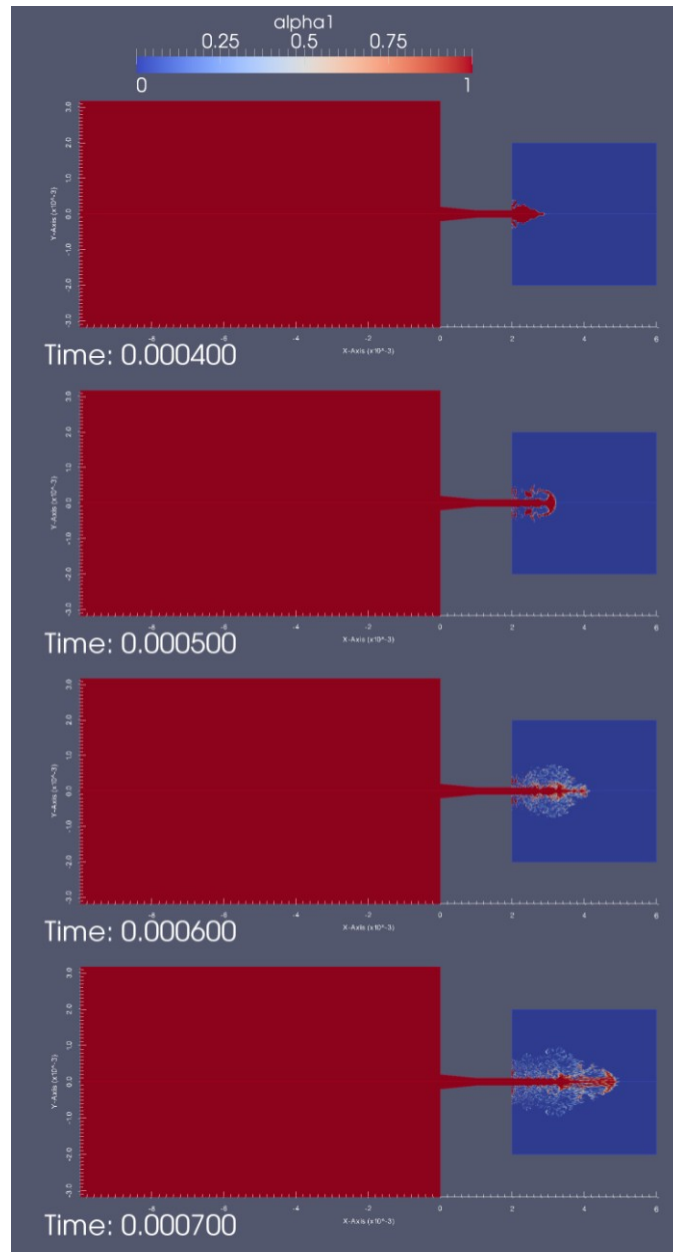


Figure 3.5. Numerical results illustrating liquid fraction of jet (courtesy of H. Nakayama)

3.2. Quantitative Assessment

The stagnation pressure is one of the fundamental measurements in this experiment as it can be used to validate the model developed in the previous chapter. Furthermore, it can also be used to determine if force emanating from the injector can deliver a

successful injection. Consequently, tracking the variation of the stagnation pressure as a function of time over the injection interval, will determine if the jet emanating from the injector is strong enough to deliver the medication, moreover it will also determine which depths and type of tissue the injector targets. Studies have shown that a minimum stagnation pressure of 3 MPa is required to penetrate the skin, this pressure is spread over the area of the injector orifice will produce very small forces. In fact typical values are less than 1.5 N, therefore it is necessary to measure these values in an extremely precise way. Furthermore, the time required to deliver an injection is usually on the order of 50 ms, depending on the volume to be delivered. This further complicates measurements of pressure, and requires a sensor with a very fine resolution and rapid response time. Obtaining the stagnation pressures in this experiment was done with the use of a Honeywell (FSG15N1A) force transducer. This transducer has a range from 0 to 1500 g and a response time of 0.1 ms, enabling measurements of the injector force to be taken accurately over time. Once the force readings are obtained it is then possible to convert these into stagnation pressure by simply dividing them by the area of the jet. The force transducer is also coupled to a signal amplifier which imposes a gain of 20 on the output voltage, which is read by a Rigol 100 MHz DS1102E oscilloscope capable of sampling 1 Giga points per second. Calibration of the force transducer is conducted by imposing known weights and plotting the voltage response of the transducer. During testing the injector is fixed within a steel vise, with stopper for proper repositioning. This ensures precise positioning of the jet relative to the force transducer.



Figure 3.6. Experimental setup of injector on force transducer

The model developed in this study has a number of parameters which can be varied in order to determine its accuracy. Nevertheless varying some of these parameters can be impractical, as it would require machining many different sizes of injectors. Consequently there are only a few specific parameters that can be varied in order to validate the model. These consist of driver pressure, nozzle diameter and injection volume. In fact these parameters are the most important in determining the penetration depth, jet velocity and subsequent jet stagnation pressure. The model was tested using five different nozzle sizes at pressure which range from 4 to 7 Bar. Table 3.1 and 3.2 summarize the various nozzle as well as the different operating pressures. The nozzles for the injectors were obtained from O'Keefe Controls Co. They are manufactured from stainless steel with a precision of 0.00254 mm.

Nozzle Size Specifications		
Nozzle Number	Diameter (μm)	Area (m^2)
N05	129.59	1.32×10^{-8}
N06	149.86	1.76×10^{-8}
N07	180.34	2.55×10^{-8}
N08	200.66	3.16×10^{-8}
N10	259.08	5.27×10^{-8}

Table 3.1. Nozzle number and size specifications

Experimental Test Parameters		
Pressure Range (Bar)	Nozzle Size	Volume
4-7	100 μm – 200 μm	0.1 ml

Table 3.2. Experimental test parameters

3.2.1. Test Procedure

In order to obtain individual pressure traces of jet stagnation pressures a specific procedure was invoked. The injector chamber volume is first adjusted to the desired volume to be delivered. The liquid to be delivered is then loaded into the chamber through the use of a syringe. This step ensures that air pockets are not trapped in the column. Once the chamber is filled then the orifice is threaded in place. The injector assembly is then positioned in the vise using the adjustment stoppers.

The driving pressure is provided by an air compressor fitted with a precision regulator. This makes it possible to accurately adjust for different pressure ranges. The maximum test pressure is kept 100 kPa below the maximum delivery pressure of the

compressor in order to ensure that pressure traces do not represent lower pressures than the target driving pressure.

Individual nozzle and pressure combinations were tested a minimum of twenty times in order to ensure consistent and reliable results. Furthermore, it was noted that varying the amount of volume did not directly influence the stagnation pressure of the jet; rather it governed the time duration of the injection. As a result, the injection volume was kept constant throughout the experiments in order to verify the effects of parameters only related to jet stagnation pressure. Moreover, the driver pressure was distributed within the aforementioned range in 1.4 Bar increments. The data for these tests was recorded and post processed in order to perform comparisons to the numerical results obtained from the model.

It is also important to note that the injection process was tracked over the first 10 ms. As previously mentioned in Chapter 1, it is the very first few milliseconds of the injection which provide a peak in pressure to penetrate the skin and deposit the medication. Therefore, in order to obtain a more accurate portrayal of the injection within these first few moments the equipment was adjusted to provide a maximum sampling rate within the initial injection period.

3.3. Results

In order to validate the model derived in Chapter 2 it is first necessary to record the stagnation pressure fluctuations with time for different nozzle and pressure combinations. These single traces must be compared to those predicted by the model in order to validate both the proper functioning of the apparatus as well as the applicability of the air

powered model. Figure 3.7 depicts one such experiment whereby a 200 micron nozzle injects 0.1 ml of fluid driven at 413 kPa. It is evident from this figure that there is clearly a pressure peak and the pressure oscillates about a mean injection pressure. As previous studies mention it is this peak which is important in the formation of a fracture in the skin and the subsequent average delivery pressure determines the depth at which the medication is delivered (Arora *et al.* 2007). The magnitude of the peak pressure and average pressure seem to agree with general results obtained from literature. It is also possible to note that the rise time to peak pressure and subsequent stabilization to the average pressure occur very rapidly. The rise to peak in most of the studied cases occurs within 0.75 ms and the stabilization to the mean pressure is within the same time frame.

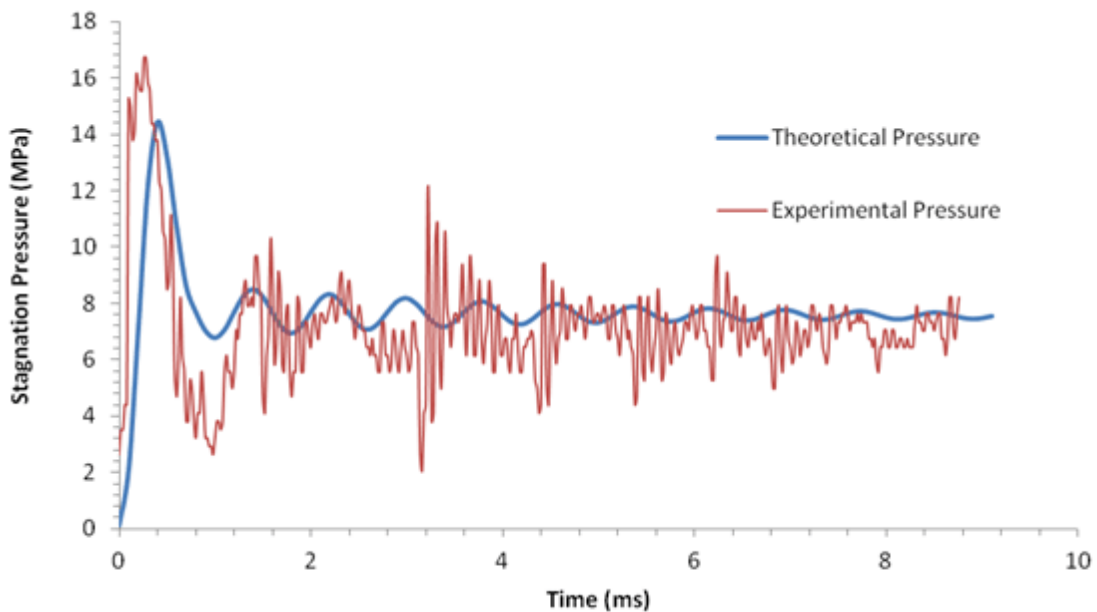


Figure 3.7. Stagnation pressure as function of injection time for 200 μm nozzle at 413 kPa

Figure 3.7 depicts a good correlation between the behaviour predicted by the model and the corresponding experimental result. It is important to note that both the peak and

the mean pressure for all cases studied are within 15% agreement with the developed model. Furthermore, Fig. 3.7 also illustrates a good match between the oscillation frequency. Despite the correlation of both experimental and theoretical data, the frequency of the oscillatory behaviour about a mean value is variable. A small number of the experiments conducted exhibited more drastic fluctuations in frequency whilst others did not oscillate and stabilized immediately after the peak to a mean value. It is also suspected that this behaviour is caused by the pressure transducer not sensing small changes as quickly as the injection progresses. Although it has a response time of 0.1 ms, the sensitivity of the device makes it difficult to acquire both rapid and minute pressure changes. Nevertheless it is only the average and peak pressure that determines the performance of the device as well as the penetration, consequently, predicting the oscillatory behaviour is of lesser importance.

The stagnation pressure also makes the computation of average velocity over the diameter of the orifice possible. This is done by using the values of stagnation pressure and dividing it over the area of the exit orifice. Figure 3.8 shows the velocity profile of the aforementioned case, it is possible to note that the peak velocity also corresponds with the 150 - 200 m/s range described in literature.

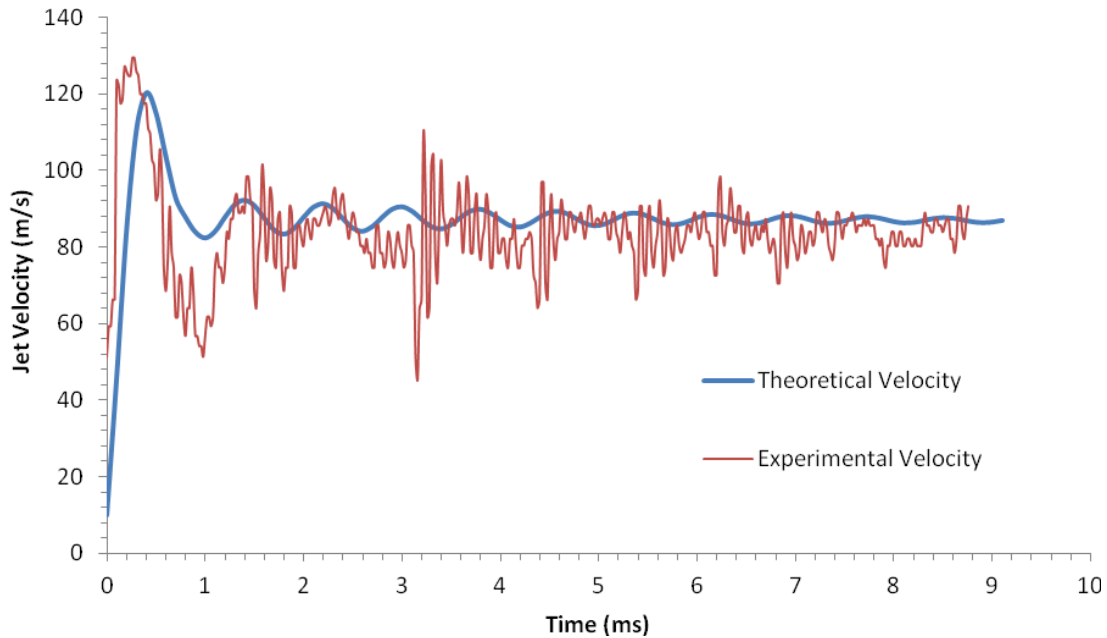


Figure 3.8. Jet velocity as a function injection time for 200 μm nozzle at 413 kPa

After benchmarking the injector and the model by analyzing the pressure time profile, it was then possible to perform a comprehensive study of all injector nozzle sizes as well as different operating pressures. Figure 3.9 depicts the peak pressure obtained from 5 different nozzles operating at 413, 550, 620 and 690 kPa, respectively. The results depict a linear increase in the peak pressure as the driver pressure is increased from 413 to 690 kPa. Furthermore the experimental data from this figure correlate very well to the theoretical model. Obtaining an average value for peak pressure for the different nozzle sizes using the air powered model made it possible to analyze the experimental data. Table 3.3 indicates that the maximum variation for the peak pressure is 15% and occurs at lower driver pressures. The greater influence of O-ring friction is a possible explanation as to the greater divergence from the theoretical average peak pressure. As O-ring friction is difficult to model because of its variability with pressure, the model seems to over compensate for this term causing the theoretical peak at lower pressures to

be less than experimental values. Compounding this error is sensitivity of the probe, a variation of 2 MPa as is the case with the low driver pressure peaks represents a force variation of 0.0264 N (2.693 g). The transducers range varies from 0 - 1500 g. Therefore a difference of 2 MPa would correspond to 0.18% of the transducers range, as a result these slight difference can be attributed to the inaccuracies of the force transducer. Nevertheless it is possible to conclude that the model is valid in predicting the peak pressures of the injector, given the injector geometry and driver pressure.

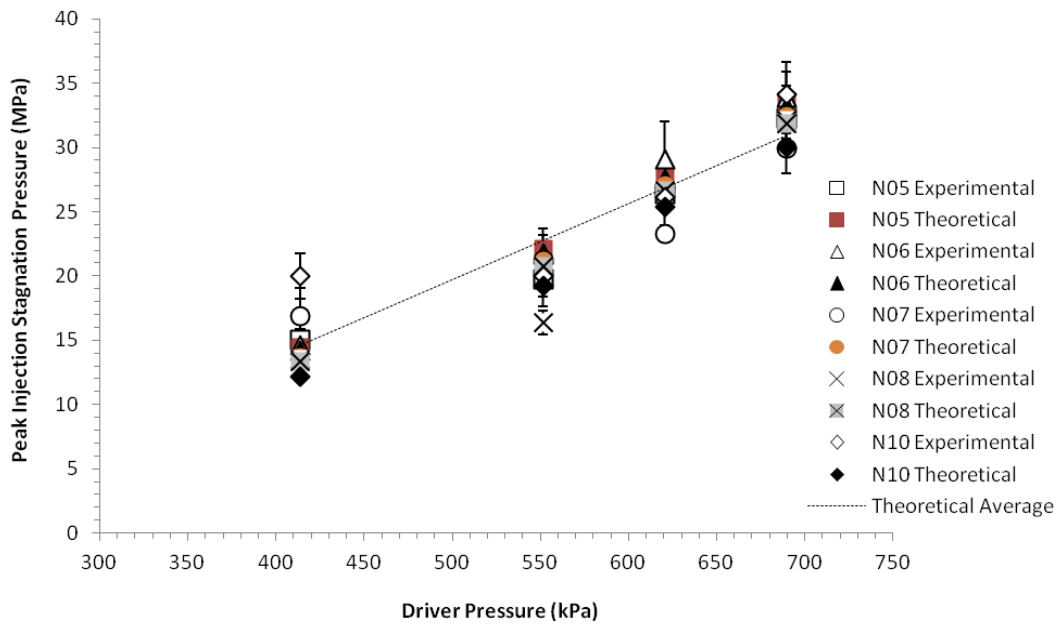


Figure 3.9. Peak stagnation pressure as a function driver pressure

Error for Peak Stagnation Pressure Measurements Based on 95% Confidence Interval					Error (MPa)
Nozzle Size	Driver Pressure				
	689 (kPa)	620 (kPa)	550 (kPa)	413 (kPa)	
N05	±1.65	±1.33	±2.08	±2.18	
N06	±2.76	±2.96	±2.04	±1.28	
N07	±1.94	±0.62	±1.92	±2.15	
N08	±2.69	±0.54	±0.93	±0.71	
N10	±1.79	±2.54	±1.57	±1.77	

Table 3.3. Error for peak stagnation pressure measurements

The average stagnation pressure reached by the injector after the pressure peak was also carefully analyzed. Figure 3.10 illustrates the variation of average injection pressure after the pressure peak, with varying nozzle diameters and driver pressure. The experiment depicts a linear increase in stagnation pressure as the driver pressure increases within the operating range, this agrees with the trend predicted by the air-powered model (as shown by the dotted line). However, it appears that the experimental data for average pressure is slightly higher than the predicted values obtained using the air powered model. Table 3.4 can be used to highlight this notion; the average pressure over the duration of the injection was obtained by finding the mean of the predicted results from the air powered model at differing nozzle sizes and fixed driver pressure. These values were then compared to the experimental data and yielded a maximum variation of ± 2.58 MPa, again occurring when lower driver pressures are utilized. Nevertheless this variation is acceptable given that the force it represents is only a small fraction of the force transducers range.

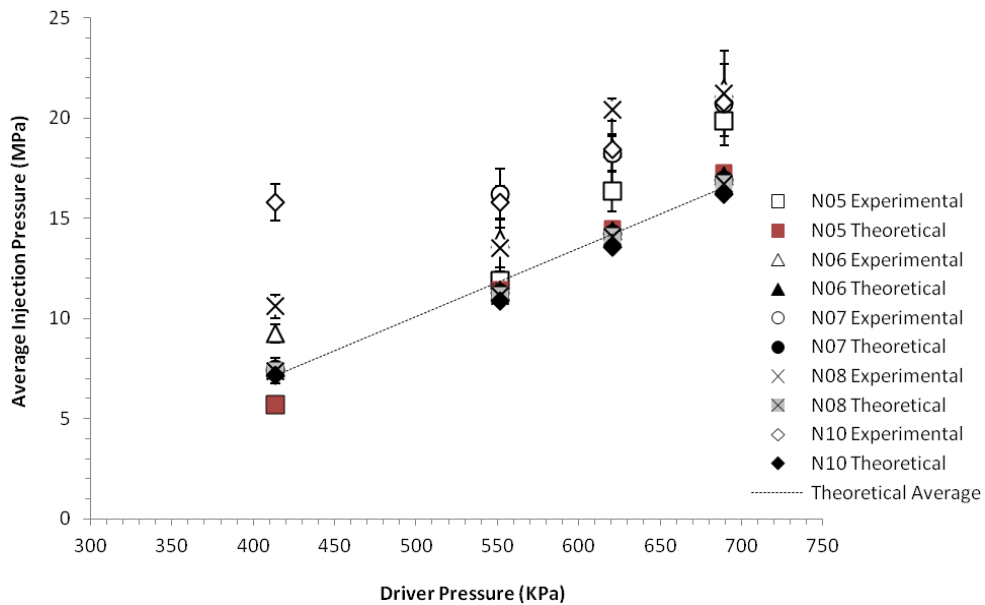


Figure 3.10. Average stagnation pressure as a function driver pressure

Error for Average Stagnation Pressure Measurements Based on 95% Confidence Interval				
Nozzle Size	Driver Pressure			
	689 (kPa)	620 (kPa)	550 (kPa)	413 (kPa)
N05	±1.22	±1.01	±0.46	±0.42
N06	±1.19	±0.68	±2.58	±0.45
N07	±0.76	±0.59	±1.25	±0.62
N08	±2.14	±0.56	±0.98	±0.58
N10	±0.77	±2.13	±0.81	±0.91

Error (MPa)

Table 3.4. Error for average stagnation pressure measurements

The results obtained from the experimental data also illustrate another very important notion. The peak pressures for different nozzles at constant driver pressures seem to approach the same value. This can be explained by analyzing the system in terms of energy. Although the area of the nozzle exit is varied, the area of the plunger remains the same which means the total energy imposed on the fluid for a given driver pressure remains the same irrespective of the exit nozzle area. If fluid damping is not present in the system then one would expect much higher velocities for smaller nozzle areas. However, fluid damping in the system causes there to be more energy dissipation for smaller nozzles due to the force required to push the fluid through a smaller exit area. Consequently, the air-powered model predicts roughly the same stagnation pressure for the tested nozzle sizes and an increase of 12 m/s in maximum jet velocity when decreasing from a 250 to 130 μm nozzle diameter. This can be confirmed by analyzing Figs. 3.11 and 3.12 which compares the stagnation pressure as a function of time, with and without fluid damping for a constant driver pressure of 413 kPa.

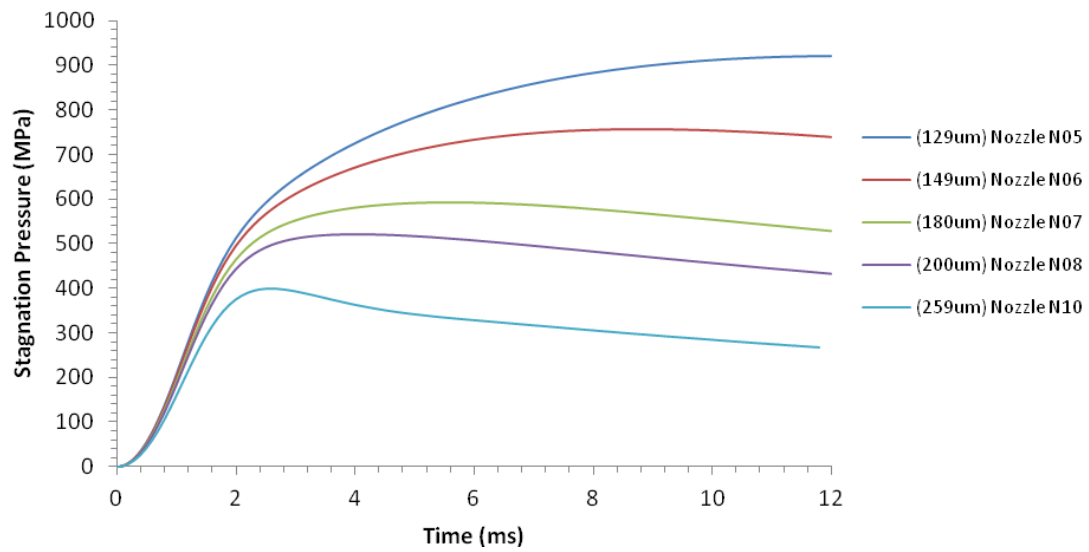


Figure 3.11. Stagnation pressure as a function time without fluid damping in the model

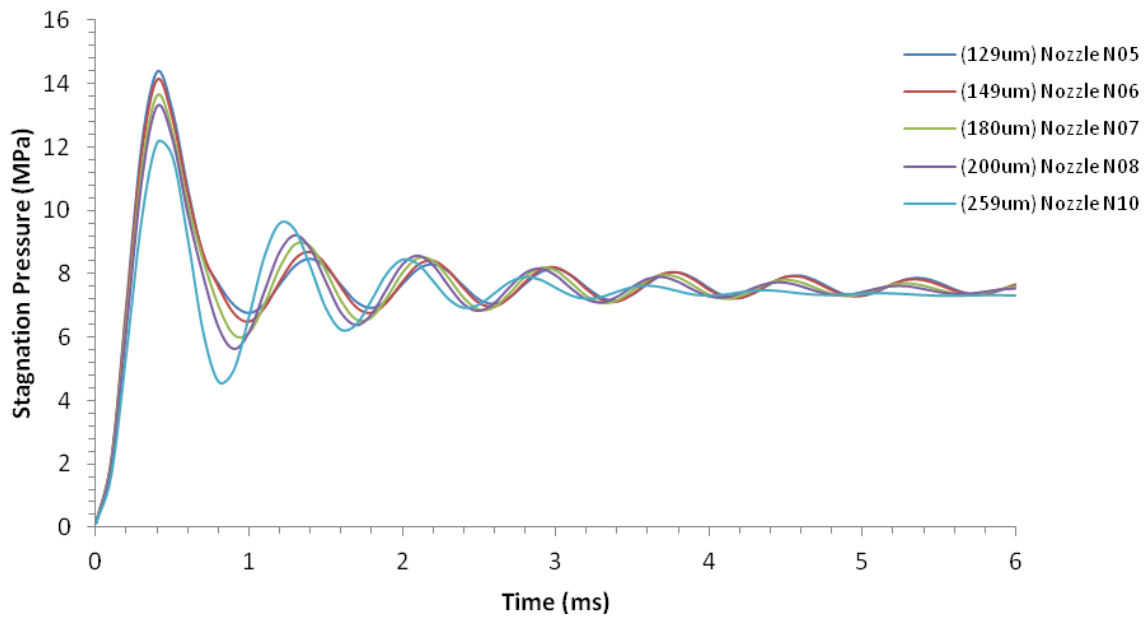


Figure 3.12. Stagnation pressure as a function time with fluid damping in the model

Figure 3.11 illustrating stagnation pressure with no fluid damping clearly exhibits a significant difference in stagnation pressure between nozzle sizes. A peak of 922 MPa is

reached for a 129 μm nozzle in contrast to a peak of 400 MPa for a 259 μm nozzle. If the chart illustrating stagnation pressure with fluid damping is analyzed as shown in Fig. 3.12 then it is possible to see that the pressure peaks for the 129 μm nozzle and the 259 μm are within 2 MPa of each other, this represents a jet velocity difference of only 12 m/s. Consequently it is possible to conclude that the decrease in area for smaller nozzles causes an increase in the energy required to overcome the damping of the fluid as it is forced through the injector orifice. Therefore it would seem that the experimental results correlate very well with their theoretical counter parts. Consequently, for the tested range of nozzle diameters, the variation on nozzle diameter has a very negligible impact on the jet stagnation pressure and velocity.

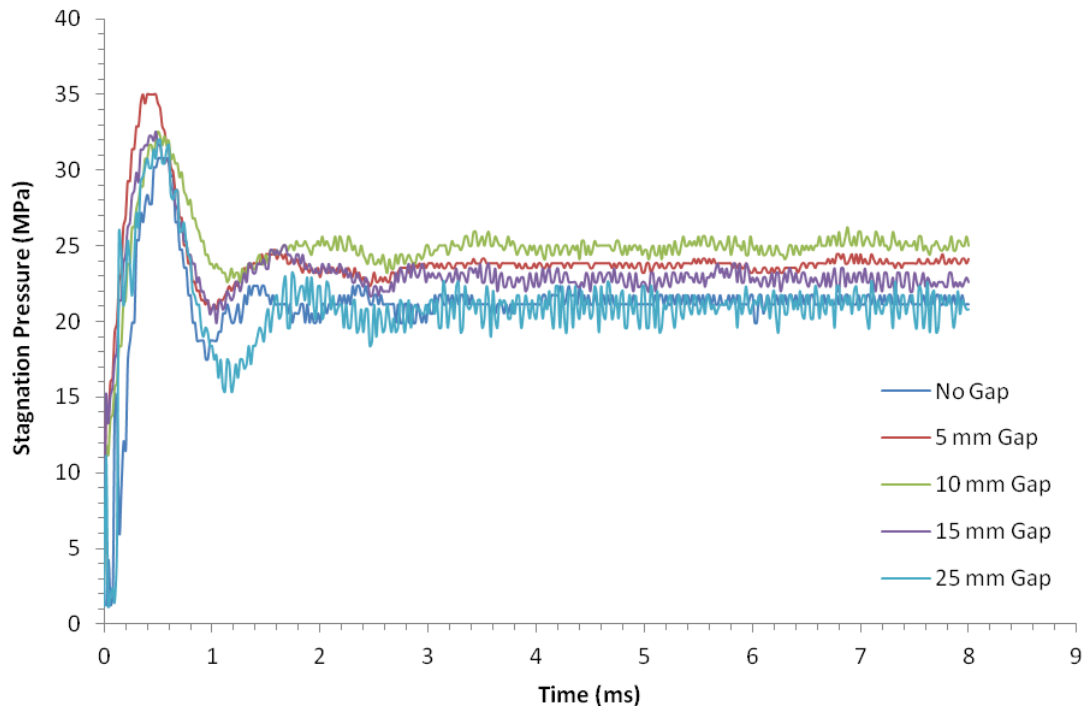


Figure 3.13. Effect of stand-off distance on stagnation pressure

Another important aspect of the results obtained is that the pressures obtained for the various experiments are not susceptible to the effect of stand-off distance. The stand-off distance can be defined as the gap between the force transducer and the nozzle exit. Figure 3.13 illustrates five different gap sizes tested with a 180 μm nozzle and at a driver pressure of 690 kPa. There is only a variation of 3.5 MPa between the peak stagnation pressures and 4 MPa for average stagnation pressures. It would seem that this variation is due not to the effect of gap distance but rather just the inherent variability of the pressure measurements. This can be confirmed if the trace illustrating the pressure profile for a 5 mm gap is compared with that of the pressure profile for a 10 mm gap. The pressure profile for the smaller gap size exhibits a slightly larger peak pressure by 2.5 MPa, however the larger gap size exhibits a 1.5 MPa increase in average stagnation pressure. If the effect of gap size was substantial then a larger gap size should see a dramatic decrease in both average and peak stagnation pressure. In fact even with a gap of 25 mm there is only a very slight decrease in these values. Consequently, the effect of stand-off distance verified within a practical working distance of up to 25 mm seems to have negligible impact on both peak and average stagnation values. It is also important to note that when the injector is used to administer medication, the nozzle will the stand-off distance will typically not exist, in other words the nozzle will come in direct contact with the skin. However, in this experiment it was not possible to have the injector contact the force transducer directly, this would result in the generation of artifacts in the force readings as illustrated in Fig. 3.14. Therefore, the effect of stand-off distance was verified to ensure that the experimental results would be unaffected by slight changes in this parameter.

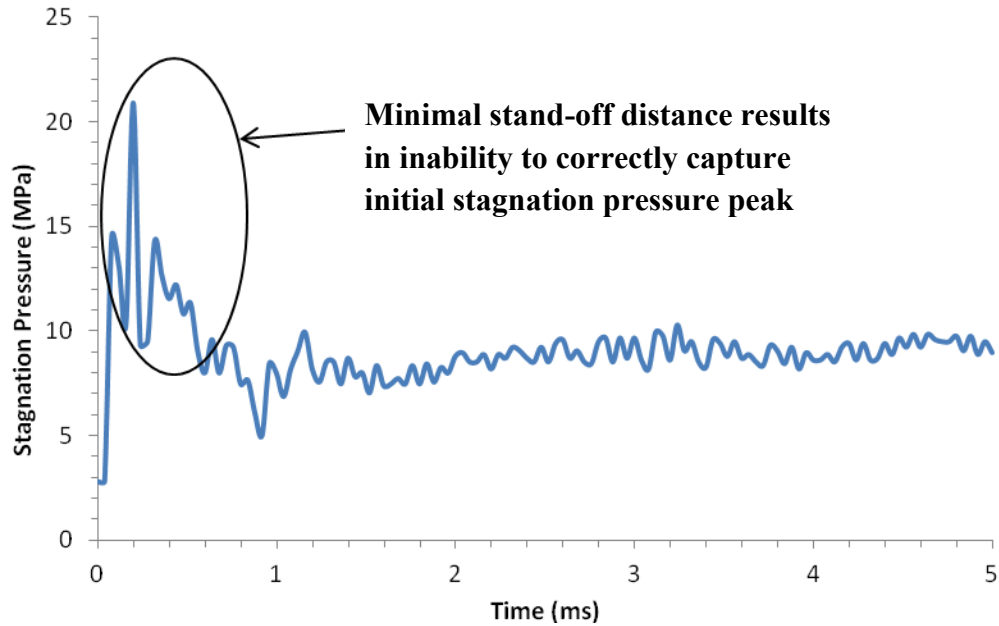


Figure 3.14. No stand-off distance causing inaccurate results

The experimental data also confirmed that the injection chamber volume does not play a significant role in impacting the peak or average stagnation pressure. Rather it seems that it affects mostly the period over which the damping occurs. Figure 3.15 illustrates the modeled differences in the injection time pressure profile for both a 25 mm and 10 mm long chamber length. The modeled results demonstrate an almost identical match in peak pressure and average stagnation pressure; however the shorter column oscillates more frequently about the average stagnation pressure than the longer column. Furthermore, there is also a time shift between the peak stagnation pressures of both column lengths. The longer column requires 0.2 ms more to reach its peak stagnation pressure than the short column. The time shift can be explained by the fact that the larger volume imparts more damping thereby shifting the peak of the injection pressure slightly. The effect of injection volume was also verified throughout these experiments. It was noted that the injection volume played a role in determining the duration of an injection.

This would agree with the model as it was shown that the chamber length has negligible effect on both peak and average stagnation pressures, then the volume injected can only affect the time period of the injection, see Fig. 3.16.

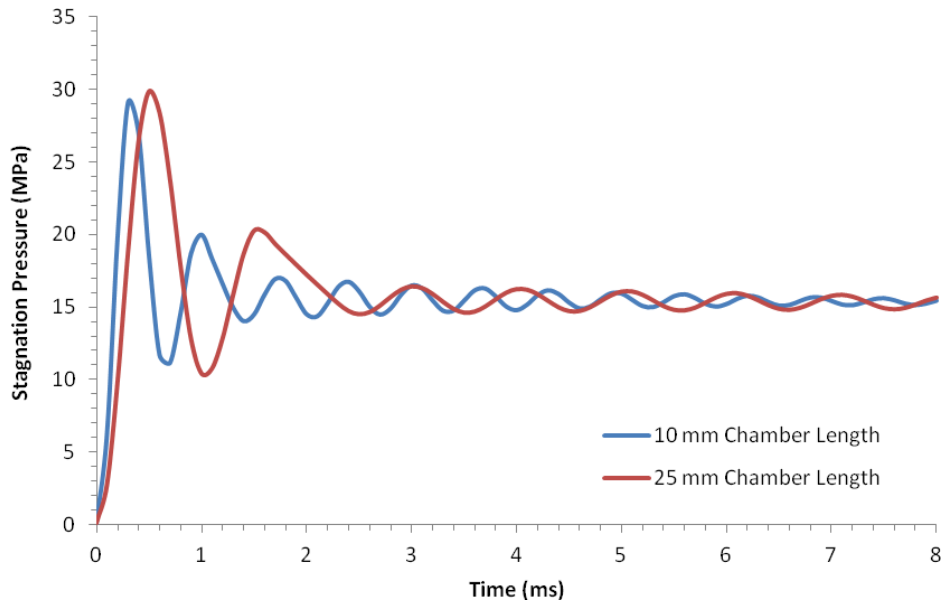


Figure 3.15. Effect of injection chamber length on stagnation pressure

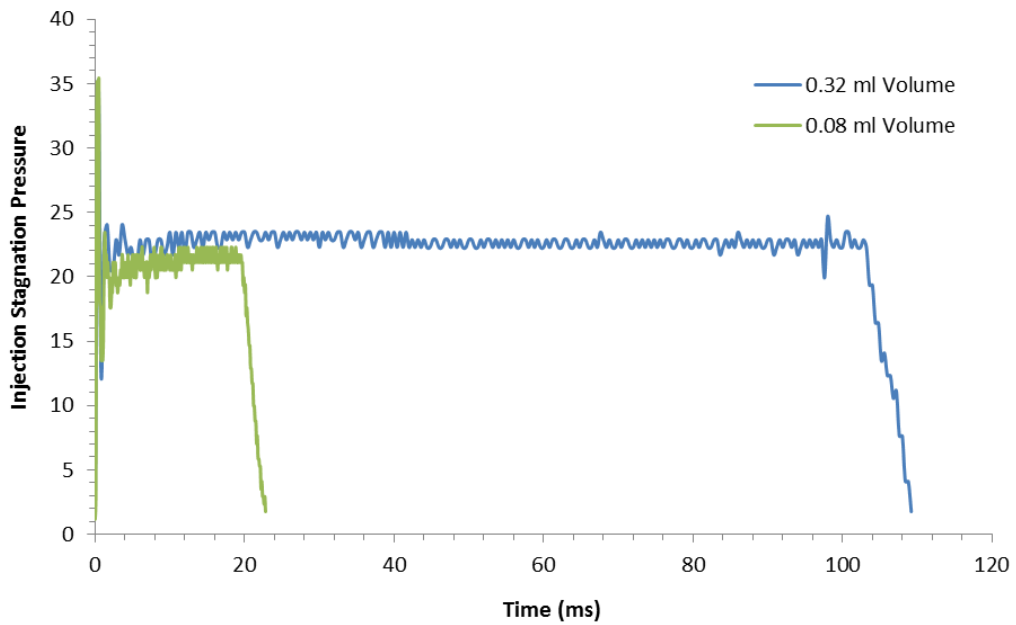


Figure 3.16. Effect of injection volume on overall injection time

In order to validate the notion that injection chamber length has a minimal effect on peak and average pressure, a 129 μm nozzle was used in conjunction with a 550 kPa driver pressure, and the injection peak and average stagnation pressures were tracked for a number of different chamber lengths. Figures 3.17 and 3.18 illustrate these results, it is possible to see that the various results for chamber lengths are scattered about the predicted model behaviour. Analyzing the error bars it is possible to see that there exists variation for some of the experimental data points. These variations are more significant for the peak stagnation pressure of longer injection chamber lengths. This can perhaps be attributed to the longer injection chamber column providing more damping at the initial phases of the injection consequently resulting in lower peak stagnation pressures. Nevertheless, the values for average stagnation pressure in Figure 3.18 agree very well with the modeled results. It is possible to conclude that as chamber length is increased from 10 mm to 40 mm there is no specific trend that emerges and the test points are scattered nearby the predicted model behaviour, illustrating that the injection chamber length has no effect on average stagnation pressure.

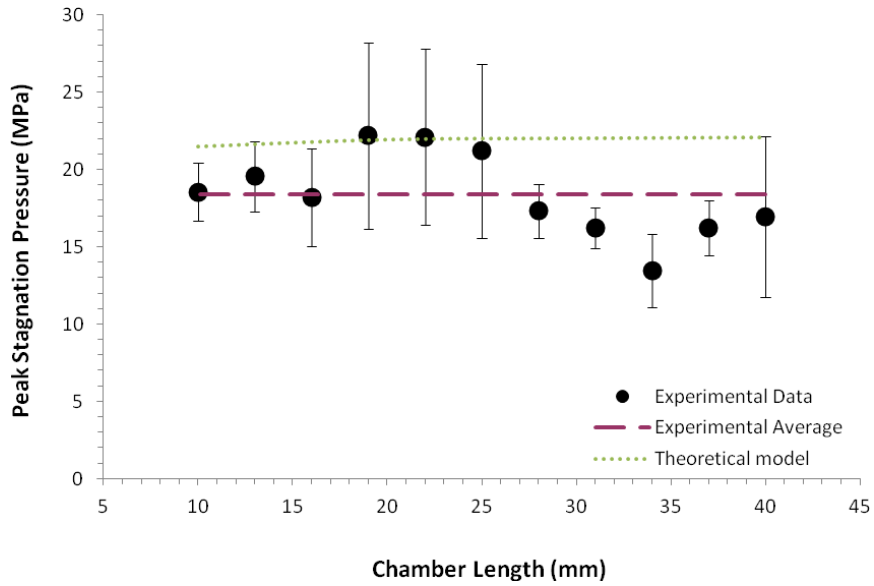


Figure 3.17. Peak stagnation pressure as a function of chamber length for 129 μm nozzle and 580 kPa driver pressure

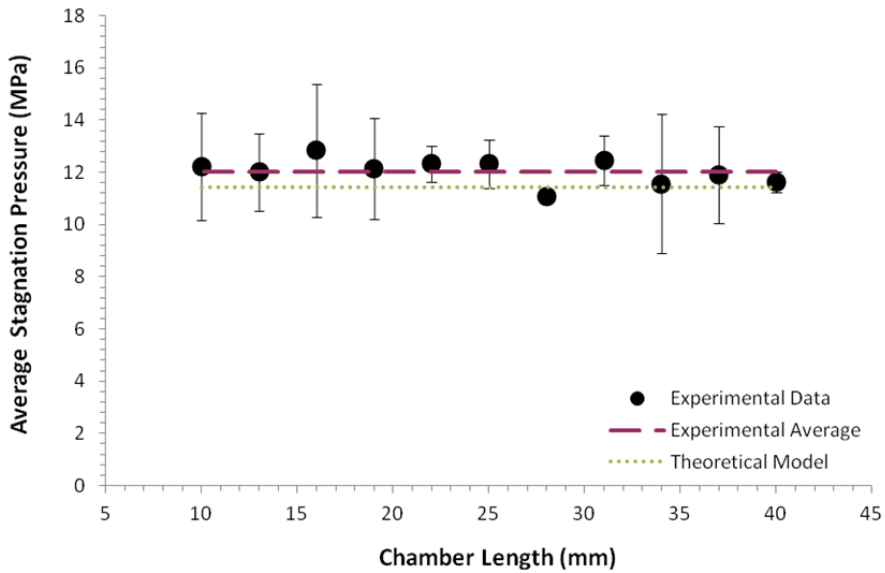


Figure 3.18. Average stagnation pressure as a function of chamber length for a 129 μm nozzle and 580 kPa driver pressure

Another important aspect of the theoretical model governing the behaviour of air-powered injectors is the influence of friction. The O-ring friction has an important influence on the magnitude of the peak and average stagnation pressures as well as the

settling time for the oscillatory behaviour of the time-pressure profile of a given injection. Figure 3.19 illustrates the modeled behaviour of friction; it is possible to see that without friction the model oscillates significantly about an average stagnation pressure, whereas at 50% friction the model settles to an average stagnation pressure much more rapidly within 2 ms of the start of the injection. Finally, the predicted model behaviour with friction settles to an average value within the first 1 ms of the injection and the peak and average stagnation values are 20% lower than those predicted without O-ring friction. It is important to note that varying the effect of O-ring friction experimentally is a difficult undertaking. This would require manufacturing several piston and driver assemblies and including different amounts of O-ring compression for each assembly. Therefore, it is much more feasible to verify the behaviour of the stagnation pressures obtained experimentally and relate these values with behaviour predicted by the air-powered model. Consequently, because the behaviour of the experimental traces is in good agreement with the model, it is possible to conclude that the model provides a reasonable estimate of mechanical friction throughout the injection process.

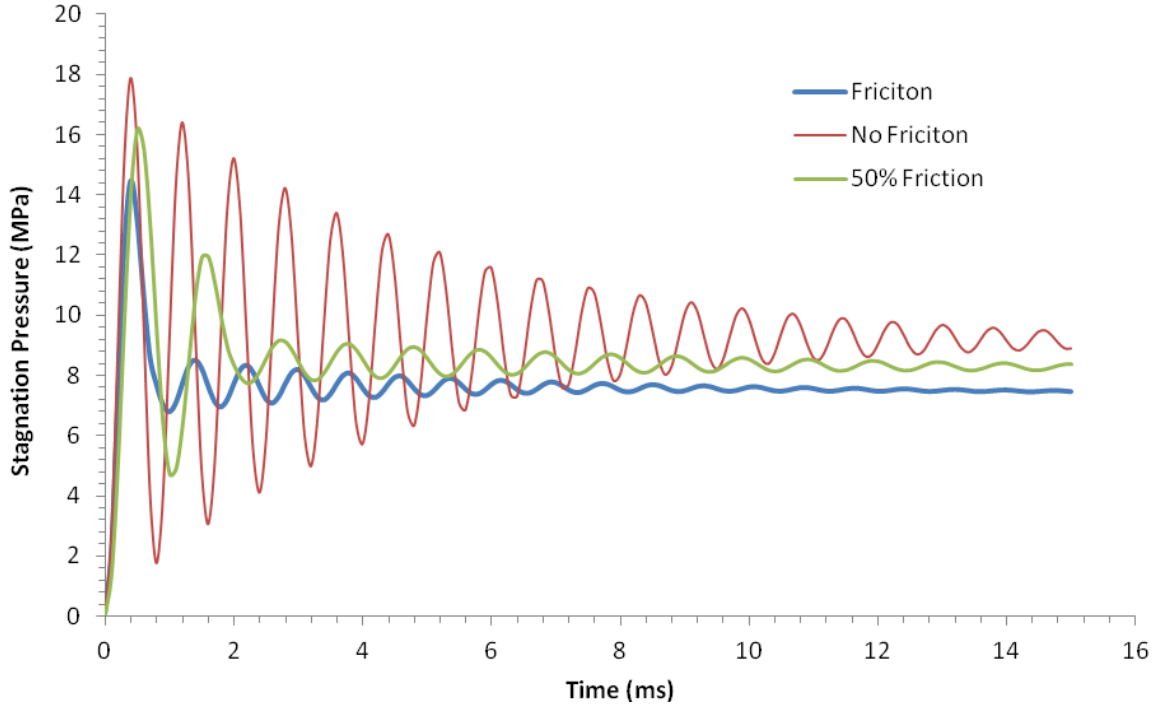


Figure 3.19. Effect of O-ring friction on stagnation pressure

The experimental results obtained in this study can be used to conclude that the air-powered model presented in this work can accurately be used to predict the peak and average stagnation pressures of gas/air powered liquid needle free jet injectors. The study verified the importance of several key parameters that will influence the performance of an air-powered injector. It was found that the stagnation pressure versus time profile with the new forcing term resembled those obtained in previous studies. There was a clear peak stagnation pressure occurring within 1 ms from the start of the injection followed by a brief oscillatory phase about an average stagnation pressure. The driving pressure was the first parameter to be studied as it defined the validity of the developed model and is critical in controlling the jet stagnation pressure. It was determined that as the driver pressure was increased both the peak and average stagnation pressure increased almost

linearly within the operating range considered. It was also determined that varying the injection nozzle diameter, whilst keeping the driver pressure constant did not have any significant impact on the peak or average stagnation pressure. It is expected that smaller diameter nozzles will produce higher speed jets and subsequently more stagnation pressure; however the decrease in diameter causes there to be more fluid damping and subsequently more energy is dissipated in the fluid for smaller diameter nozzles. This result demonstrates that for the tested nozzle ranges the stagnation pressure for all nozzle sizes at given driver pressure was approximately equal. The effect of chamber length was another key parameter studied. The chamber length was varied whilst holding other parameters fixed, and it was observed that there was no significant affect on peak or average stagnation pressure. However, the length of the fluid column did affect the oscillatory behaviour about the average stagnation pressure. It was determined that longer chamber length requires fractionally more time to reach a peak pressure and exhibits a longer period for an individual oscillation than short chamber lengths. The general experimental results obtained throughout this study agree very closely with the developed model. Consequently, it is possible to conclude that the model is valid and can accurately predict the characteristics of the jet emanating from an air-powered needle free injector.

Chapter 4. Conclusion

4.1. Concluding Remarks

This study has made it possible to develop and validate a model to predict the behaviour of the liquid jet for air powered needle free injectors. This was accomplished by first performing a detailed analysis on commercially available units and designing and fabricating a custom injector that allows the variation of several parameters which are usually fixed. This prototype then made it possible to validate a model constructed based on previous work from Baker and Sanders (1999). The model developed in this study is the first of its kind to use a forcing term that relates the air pressure used to drive the injection to the stagnation pressures of the jet exiting the injector. This addition made it possible to verify which parameters most significantly impact the peak and average stagnation pressures for air powered injectors.

The air-powered model developed in this study proved extremely useful in predicting the stagnation pressure and jet velocity of the liquid stream exiting the injector. However, it was noted that there exists some variation in stagnation pressure predicted by the model. This can be attributed to many causes such as the mechanical friction caused by O-rings which have a tendency to change depending on the amount of lubrication and relaxation. Furthermore, the displacement of the plunger assembly is dependent on many factors such as the pressure in the driving chamber as well as the damping force imposed by the fluid. In order to deliver more constant and accurate injections it is necessary to decouple the displacement of the plunger assembly from the fluid damping and mechanical friction. In other words, future work should be focused on developing power

sources that are capable of delivering an injection in a controllable manner, in which the time-pressure profile is not fixed but rather can be adjusted as the injection progresses. There are a number of ways to do this; recently Lorentz force actuators as well as piezoelectric crystals have been used to eject the liquid in a controllable manner (e.g., Stachowiak et al. 2007; Taberner et al. 2012). However research is still required in order to determine the ideal injection profile, as well as finding way to correlate the injection stagnation pressure to jet penetration. If these challenges are overcome it will be possible to minimize the role of the hypodermic needle and have a more effective and pain free way of delivering medication.

4.2. Contribution to Knowledge

This study has made several key contributions to needle free injector technology. The first is the development and validation of a new model for air-powered injectors that can be used to accurately predict the stagnation pressure and jet velocity of the liquid stream exiting the injector. This is of great importance for needle free injectors as these parameters determine how deep the medication can be delivered as well as the effectiveness of delivery based on the jet power. This study also made it possible to develop a platform for testing air powered needle free injectors. The research conducted on commercially available units made it possible to create a prototype injector with variable parameters that can now be used to verify the influence of improvements to plunger, nozzle and driver designs.

References

1. H. Alexander, D.L. Miller, "Determining skin thickness with pulsed ultra sound," *J. Invest. Dermatol.*, Vol. 72, pp. 17-19, 1979
2. A. Arora, I. Hakim, J. Baxter, R. Rathnasingham, R. Srinivasan, S. Mitragotri, "Needle free delivery of macromolecules across the skin by nanolitre-volume pulsed microjets," *Proc. Nat. Acad. Sci.*, Vol. 104(11), pp. 4255–4260, March 2007.
3. A.B. Baker, J.E. Sanders, "Fluid mechanics analysis of a spring- loaded jet injector," *IEEE Trans. Biomed. Eng.*, Vol. 26(2), pp. 235-242, Feb. 1999.
4. M. Bermejo, I. Gonzalez-Alvarez, "How and where are drugs absorbed?" In: *Preclinical Development Handbook: ADME and biopharmaceutical properties*, Edited by S.C. Gad, John Wiley & Sons Inc, NJ, USA, 2008.
5. M.B. Brown, G.P. Martin, S.A. Jones, F.K. Akomeah, "Dermal and transdermal drug delivery systems: current and future prospects," *Drug Deliv.* Vol. 13 pp. 175-187, 2006.
6. K. Chen, H. Zhou, J. Li, G.J. Cheng, "Stagnation pressure in liquid needle-free injection: modeling and experimental validation," *Drug Deliv. Letters*, Vol. 1, pp. 97-104, 2011.
7. Darcoid Norcal Seals., "O-ring load per linear inch of seal empirical chart" (www.darcoid.com/images/uploads/pdfs/empiricalcharts)
8. T.H. Guang, D.T. Wang, "*Operation Manual of Sealing Components*," Mechanical Industry Press, Beijing, China, 1994.
9. K. Kelly, A. Loskutov, D. Zehrunge, K. Puaa, P. LaBarre, N. Muller, W. Guiqiang, H.G. Ding, D. Hu, W.C. Blackwelder, "Preventing contamination between injections with multiple-use nozzle needle-free injectors: A safety trial," *Vaccine*, Vol. 26, pp. 1344-1352, March 2008.
10. M.A. Kendall, "Needle free vaccine injection," in *Handbook of Experimental Pharmacology*, Springer-Verlag, Berlin Heidelberg, Ch. 3, pp. 194-215, 2010.
11. P.A.J. Kolarsick, M.A. Kolarsick, C. Goodwin, "Anatomy and physiology of the skin," *J. Dermatol. Nurse Assoc.*, Vol. 3(4), pp. 203-213, August 2011.
12. Y. Liu, "Utilization of the Venturi effect to introduce micro-particles for epidermal vaccination," *Med. Eng. Phys.*, Vol. 29, pp. 390-397, 2007.
13. J.A. McGrath, R.A.J. Eady, F.M. Pope, "Anatomy and organization of human skin," In: *Rook's Text Book of Dermatology*, 7th Edition, Chap. 3, Blackwell Publishing, Inc., Malden, MA, USA, 2010.

14. S. Mitragotri, "Immunization without needles," *Nature Reviews. Immunology*, Vol. 5, pp. 905-917, Dec. 2005.
15. S. Mitragotri, "Current status and future prospects of needle free liquid jet injectors," *Nature Reviews. Drug Discovery*, Vol. 5, pp. 543-548, July 2006.
16. C. Mohanty, P. Chandana, C.D. Mannavathy, D. Srikanth, and R. Tabassum, "Needle free drug delivery systems: A review," *Int. J. Pharmaceutical Research Development (IJPRD)*, Vol. 3(7) pp. 7-15, Oct. 2011.
17. H. Nakayama, R. Portaro, H.D. Ng, "CFD Investigation of high speed liquid jets emitted from needle free jet injectors," Submitted to the 21st Annual Conference of the CFD Society of Canada, Sherbrooke, Quebec, May 6-9, 2013.
18. OpenCFD, "*OpenFOAM, The Open Source CFD Toolbox*," OpenCFD Ltd. 2009.
19. R. Portaro, A.L. Gunter, H.D. Ng, "Analysis of high speed liquid jets emitted from needle free jet injectors," 65th Annual Meeting of the APS Division of Fluid Dynamics, in San Diego, CA, USA, Nov. 18-20, 2012
20. J. Schramm-Baxter, S. Mitragotri, "Needle-free jet injections: dependence of jet penetration and dispersion in the skin on jet power," *J. Control. Release*, Vol. 97, pp. 527-535, July 2004.
21. W. Seehanam, W. Sittiwong, K. Pianthong, A. Matthujak, "Investigation of high speed liquid jet using computational fluid dynamics," *Proc. of the 23rd Conf. Mech. Eng. Network of Thailand*, Chiang Mai, Nov. 4-7, 2009.
22. H.J. Sneek, J. H. Vohr, "Hydrodynamic lubrication: Fluid film lubrication" In: *CRC Hand Book of Lubrication: Theory and Practice of Tribology*, Edited by E.R. Booser, CRC Press LLC, NY, USA, 1983.
23. O.A. Shergold, N.A. Fleck, T.S. King, "The penetration of a soft solid by a liquid jet, with application to the administration of a needle-free injection," *J. Biomech.*, Vol. 39, pp. 2593-2602, 2006.
24. J.C. Stachowiak, M.G. von Muhlen, T.H. Li, "Piezoelectric control of needle free transdermal drug delivery," *J. Control. Release*, Vol. 124, pp. 88-97, Aug. 2007.
25. A. Taberner, N.C. Hogan, I.W. Hunter, "Needle-free jet injection using real-time controlled linear Lorentz-force actuators," *Med. Eng. Phys.* Vol. 34(9), pp. 1228-1235, Nov. 2012.
26. Y. Tagawa, N. Oudalov, C.W. Visser, I.R. Peters, D. van der Meer, C. Sun, A. Prosperetti, D. Lohse, "Highly focused supersonic microjets," *Phs. Rev. X*, Vol. 2, 031002 (10 pages), July 2012.
27. Tev-Tropin Inc., "*T-Jet Schematic Diagram*," (<http://www.tev-tropin.com/tjet/>)

Appendix. Sample of Data Processing

The following calculation demonstrates an example of the error analysis for pressure measurements. Table A1 below shows a sample peak stagnation pressure measurement for one experimental condition.

Test #	Peak Stagnation Pressure (MPa)
1	32.00
2	28.14
3	35.90
4	35.96
5	36.78
6	28.67
7	21.92
8	30.79
9	31.96
10	35.77
11	31.38
12	36.36
13	35.48
14	29.62
15	32.55
16	30.50
17	32.54
18	33.13
19	34.31
20	32.70

Table A.1. Measurement of peak stagnation pressure for 129 μm nozzle and at 689 kPa driver pressure

Using the data given in the Table A.1, the following statistical quantities can be calculated:

$$\text{Average}(\bar{x}) = \frac{\sum x}{n} = 32.30 \text{ MPa}$$

$$\text{Expected Average from Model } (\mu) = 33.63 \text{ MPa}$$

$$\text{Standard Deviation } (\sigma) = \sqrt{\frac{\sum (x - \bar{x})^2}{n - 1}} = 3.666 \text{ MPa}$$

$$Z = \frac{\bar{x} - \mu}{\sigma / \sqrt{n}}$$

Using the normal distribution it is possible to obtain a value for Z when a 95% confidence interval is required of which the probability function is:

$$P(-z \leq Z \leq z) = \pm 1.96$$

The limits for error can then be computed taking the value for 95% of the area under the normal distribution and multiplying by the standard error.

$$\text{Error} = \pm 1.96 \frac{\sigma}{\sqrt{n}} = 1.65 \text{ MPa}$$